Monthly Notices
of the
ROYAL ASTRONOMICAL SOCIETY

MNRAS **459,** 178–198 (2016)
Advance Access publication 2016 March 8

doi:10.1093/mnras/stw551

Radio polarization maps of shell-type supernova remnants – I. Effects of a random magnetic field component and thin-shell models

R. Bandiera[1]★ and O. Petruk[2]

[1]*INAF – Osservatorio Astrofisico di Arcetri, Largo E. Fermi 5, I-50125 Firenze, Italy*
[2]*Institute for Applied Problems in Mechanics and Mathematics, Naukova Street, 3-b Lviv 79060, Ukraine*

Accepted 2016 March 3. Received 2016 February 28; in original form 2015 December 15

ABSTRACT

The maps of intensity and polarization of the radio synchrotron emission from shell-type supernova remnants (SNRs) contain a considerable amount of information, although of not easy interpretation. With the aim of deriving constraints on the 3D spatial distribution of the emissivity, as well as on the structure of both ordered and random magnetic fields (MFs), we present here a scheme to model maps of the emission and polarization in SNRs. We first generalize the classical treatment of the synchrotron emission to the case in which the MF is composed of an ordered MF plus an isotropic random component, with arbitrary relative strengths. For a power-law particle energy distribution, we derive analytic formulae that formally resemble those for the classical case. We also treat the shock compression of a fully random upstream field and we predict that the polarization fraction in this case should be higher than typically measured in SNRs. We implement the above treatment into a code, which simulates the observed polarized emission of an emitting shell, taking into account also the effect of the internal Faraday rotation. Finally, we show simulated maps for different orientations with respect to the observer, levels of the turbulent MF component, Faraday rotation levels, distributions of the emissivity (either barrel-shaped or limited to polar caps) and geometries for the ordered MF component (either tangential to the shell or radial). Their analysis allows us to outline properties useful for the interpretation of radio intensity and polarization maps.

Key words: acceleration of particles – magnetic fields – polarization – radiation mechanisms: non-thermal – ISM: supernova remnants – radio continuum: general.

1 INTRODUCTION

Supernova remnants (SNRs), an aftermath of stellar explosions, were among the first sources to be observed by radio astronomers and, since the advent of radio interferometers, many of them have been mapped with high spatial resolution. Their typical shell-like emission pattern roughly traces the location where the blast wave of the explosion hits the ambient medium. In many cases, radio detectors have been devised to provide the observer with full information about the incoming polarized radiation (i.e. all four Stokes parameters).

In spite of this wealth of information, it seems that radio observations of SNRs have not been fully exploited, at least if compared with observations in other spectral bands, like for instance in X-rays. One possible reason is that the radio emissivity, which in SNRs is typically non-thermal and of synchrotron origin, depends on a combination of physical parameters that are separately poorly known, namely the injection efficiency of the relativistic electrons and the magnitude of the magnetic fields (MFs).

On the other hand, the spatial structure of the polarization may provide important clues on the geometrical structure of the MF. For instance, it was noted (Milne 1987) that there is a tendency in younger SNRs for the polarization to be consistent with a predominantly radial structure of the MF, while in older SNRs the MF structure is predominantly tangential to the SNR boundary. A review of this can be found in Dubner & Giacani (2015). This kind of dichotomy has been interpreted by some authors (e.g. Jun & Norman 1996; Inoue et al. 2013) as evidence that in younger SNRs, instabilities lead to strongly tangled MFs. Instead, in older SNRs the ordered component of the MF still keeps a memory of the pattern originated by the shock compression of the ambient MF. It has also been shown (Petruk, Kuzyo & Beshley 2016) that in post-adiabatic SNRs, the parallel component of the MF decreases, while the perpendicular one increases in the shock downstream. Therefore, shocks of different obliquities in old SNRs tend eventually to become quasi-perpendicular, even those that initially were quasi-parallel.

★ E-mail: bandiera@arcetri.astro.it

MF turbulent amplification generated by kinetic processes for a quasi-parallel shock (e.g. Caprioli & Spitkovsky 2014b, and reference therein) should give rise to a tangential ordered component. In fact, efficient MF amplification taking place upstream of the shock leads, in the most extreme case, to a completely random MF, but then the shock compresses this field, enhancing the tangential component with respect to the radial one. Therefore, the observation of radially oriented MFs cannot be justified even in this case, but suggests instead the onset of hydrodynamic instabilities, like Rayleigh–Taylor instabilities (e.g. Jun & Norman 1996) or Richtmyer–Meshkov instabilities (e.g. Inoue et al. 2013).

Observations show that the polarization fractions vary from object to object, and from region to region within the same object, but their typical values are much lower than the maximum theoretically allowed limit ($\simeq 69$ per cent, for a slope -0.5 of the synchrotron emission, namely a slope -2.0 in the energy distribution of the emitting electrons). For instance, Dickel & Milne (1976) quote generally low polarizations, usually <10 per cent, while Kothes et al. (2006) show that the peaks of the polarization fraction typically range from about 10 per cent to about 50 per cent. This seems to indicate that the discrepancy between theory and observations can be partly explained with the superposition, along the line of sight, of regions where the MFs have different orientations, and/or with the presence of a partially random MF.

This work presents a detailed treatment of synchrotron emission for a partially random MF, and implements it within a thin-shell SNR model. This approximation allows us to simplify considerably the problem (also making our numerical models much lighter to compute), while retaining a large number of effects, and therefore, allowing an analysis of a wide variety of realistic cases. Since our aim is to show how quantitative information could be effectively extracted from (suitably detailed) polarization maps, but not to model specific sources, we will discuss here only simple geometries.

The plan of the paper is as follows.

Section 2 analyses the synchrotron emissivity and its polarization properties. We begin by reviewing the classical approach, valid for particles with a power-law energy distribution (as is typically the case for radio-emitting particles) sitting in a uniform MF. We then introduce a generalization of this approach, which extends its validity to a partially disordered MF, with the random component assumed to be isotropic. This treatment allows a continuity from an almost uniform MF to an almost completely randomized one. In a similar way, we also estimate the level of polarization induced by the compression, at a shock front, of an originally fully random MF. Just a feel is given of the difficulties that arise if the particle distribution is not a power-law, by considering the mono-energetic case.

To compare the modelling of radio polarization maps with actual observations, it is necessary to sum properly the local emissivity in the various Stokes parameters, by also correcting for the Faraday rotation (FR) effects. While this could apply to many different classes of astrophysical sources, in Section 3 we focus on radio shell-type SNRs, with suitable assumptions on the geometry of the MF as well as on the spatial distribution of thermal gas and the emitting particles. In particular, we assume axial symmetry, and the thin-layer simplified approach, deriving formulae that we then extensively use in our modelling. At the end of this section, we also present a momentum approach, which allows us to treat formally also a more general source structure, in the limit of sufficiently short radiation wavelengths.

In Section 4, we present a variety of simulated maps obtained under different parameter choices, and we use them to discuss, for instance, the effects of changing the aspect angle, the level of internal FR and the level of MF fluctuations.

In addition to the classical case, in which the ordered MF component has a meridional structure, consistent with the compression of a pre-existing uniform ambient MF, in Section 5 we also investigate a completely different case, probably more appropriate for some young SNRs, in which the observed MF structure is mostly radial. We compare some of our results with the observed structure of the SNR SN 1006.

Section 6 concludes.

2 LOCAL EMISSIVITY AND POLARIZATION

In this section, we study the synchrotron emissivity, from an element of volume. The meaning of adding the word 'radio' is that we consider only the case in which the energy distribution of the relevant electrons is a pure power law, as it is typically for radio emission. For X-ray-emitting electrons, instead, their energy distribution experiences a cut-off, which would require a different treatment from that presented below.

2.1 The classical uniform MF

Let us begin with a review of the basic formulae for synchrotron radiation and polarized radiation in general (see e.g. Rybicki & Lightman 1979). Let us first consider a particle with a given Lorentz factor γ, moving in a MF $\boldsymbol{B}$ (assumed to be uniform, at least on scales smaller than the particle gyration radius). In this case, the synchrotron power emitted per unit frequency [$\omega = 2\pi\nu$, so that $P(\nu) = 2\pi P(\omega)$] is the sum of polarized components, respectively perpendicular and parallel to the direction of the projected MF, which are equal to

$$P_{\perp}(\omega) = \frac{\sqrt{3}\, e^3 B_{\perp}}{4\pi\, m_{\rm e} c^2}\, (F(x) + G(x)) \tag{1}$$

and

$$P_{\parallel}(\omega) = \frac{\sqrt{3}\, e^3 B_{\perp}}{4\pi\, m_{\rm e} c^2}\, (F(x) - G(x))\,, \tag{2}$$

where

$$F(x) = x \int_x^{\infty} K_{5/3}(z)\, {\rm d}z \tag{3}$$

and

$$G(x) = x K_{2/3}(x), \tag{4}$$

with $K_n(z)$ being a modified Bessel function of the second kind, and

$$x = \frac{\omega}{\omega_{\rm c}} = \frac{2}{3}\frac{m_{\rm e} c}{e B_{\perp}}\frac{\omega}{\gamma^2} \mathrel{\hat{=}} \frac{2K}{B_{\perp}\gamma^2}, \tag{5}$$

where the constant K is defined by the last equation. The symbol $\mathrel{\hat{=}}$ will be used to indicate the definition of a new quantity, rather than a result. $B_{\perp}$ is the modulus of the projected MF. Note that all formulae depend only on the projected MF, while the component radial to the observer does not affect the emission (it could be investigated only through propagation effects, namely through FR).

It is more convenient to express this emission in terms of the Stokes parameters. To be more precise, now we consider only their local values, namely their values per unit path. The actual Stokes parameters (namely those that should match the observations) will

be obtained by integration along the line of sight. The choice of reference orientation for the linear polarization parameters, Q and U, is such that:

$$Q = \left\langle E_x E_x^* \right\rangle - \left\langle E_y E_y^* \right\rangle \tag{6}$$

and

$$U = \left\langle E_x E_y^* \right\rangle + \left\langle E_y E_x^* \right\rangle, \tag{7}$$

where E_x and E_y are the components of the complex amplitude of the electric vector.

Without loss of generality, let us first consider an orientation of axes with the unit vector $\hat{x}'$ perpendicular to $B_\perp$ and $\hat{y}'$ parallel to it. In this way, the parameters $\mathcal{I}'$ (total flux) and $\mathcal{Q}'$ (difference between the linear polarizations along the two axes) relative to the emission of a single particle are

$$\mathcal{I}'(\omega) = \frac{P_\perp + P_\parallel}{4\pi} = \frac{\sqrt{3}\, e^3 B_\perp}{8\pi^2 m_\mathrm{e} c^2} F(x) \mathrel{\hat{=}} H B_\perp F(x) \tag{8}$$

and

$$\mathcal{Q}'(\omega) = \frac{P_\perp - P_\parallel}{4\pi} = \frac{\sqrt{3}\, e^3 B_\perp}{8\pi^2 m_\mathrm{e} c^2} G(x) \mathrel{\hat{=}} H B_\perp G(x), \tag{9}$$

where the quantity H is defined by the rightmost equalities. Note that the Stokes parameters associated with tilted linear polarization ($\mathcal{U}'$) and circular polarization ($\mathcal{V}'$) both vanish.

For any other reference frame x–y, rotated by an angle χ (taken to be anticlockwise) with respect to the x'–y' reference frame chosen above, the Stokes parameters transform as

$$\begin{cases} \mathcal{I} = \mathcal{I}', \\ \mathcal{Q} = \ \cos(2\chi)\mathcal{Q}' + \sin(2\chi)\mathcal{U}' = \ \cos(2\chi)\mathcal{Q}', \\ \mathcal{U} = -\sin(2\chi)\mathcal{Q}' + \cos(2\chi)\mathcal{U}' = -\sin(2\chi)\mathcal{Q}', \\ \mathcal{V} = \mathcal{V}' = 0. \end{cases} \tag{10}$$

In terms of the MF components, we can write

$$\begin{cases} \cos(2\chi) = \dfrac{B_y^2 - B_x^2}{B_\perp^2}, \\ \sin(2\chi) = \dfrac{2 B_x B_y}{B_\perp^2}, \end{cases} \tag{11}$$

where $B_\perp^2 = B_x^2 + B_y^2$. For a power-law energy distribution:

$$n(\gamma) = A\gamma^{-s} \tag{12}$$

for the emitting particles, the known formulae for the emissivities (per unit volume) are recovered after integration over γ:

$$\mathcal{I}'_\mathrm{PL}(\omega) = \frac{s + 7/3}{s+1} W_\mathrm{o} B_\perp^{(s+1)/2} \tag{13}$$

and

$$\mathcal{Q}'_\mathrm{PL}(\omega) = W_\mathrm{o} B_\perp^{(s+1)/2}, \tag{14}$$

where

$$W_\mathrm{o} = \frac{AH}{4K^{(s-1)/2}} \Gamma\left(\frac{s}{4} + \frac{7}{12}\right) \Gamma\left(\frac{s}{4} - \frac{1}{12}\right). \tag{15}$$

$\mathcal{I}_\mathrm{PL}$ and $\mathcal{Q}_\mathrm{PL}$ are obtained with a rotation by an angle χ, according to equations (10). In this case, the polarization fraction is

$$\Pi_\mathrm{max} = \frac{\sqrt{\mathcal{Q}_\mathrm{PL}^2 + \mathcal{U}_\mathrm{PL}^2}}{\mathcal{I}_\mathrm{PL}} = \left|\frac{\mathcal{Q}'_\mathrm{PL}}{\mathcal{I}'_\mathrm{PL}}\right| = \frac{s+1}{s+7/3}. \tag{16}$$

So far, the distinction between primed and unprimed Stokes parameters has been just formal. However, starting from the next section, it will become more substantial. With a MF varying in time, the primed reference frame, which is instantaneously oriented with the MF, also changes its orientation with time, and therefore, the primed Stokes parameters can only appear, as instantaneous values, inside the integrals that we will use to estimate quantities averaged over fluctuations.

2.2 Inclusion of an isotropic random MF

The scope of this section is to extend the classical treatment of the synchrotron emission to the case in which the MF is a combination of an ordered component and a random component. While the two limit cases of a uniform MF (maximally anisotropic emissivity and maximal polarization fraction) and a completely random MF (isotropic and unpolarized emission) are well known, the intermediate cases are not so obvious. In particular, it must be clear that for a partly random MF, it would be incorrect to estimate the time-averaged synchrotron emissivity as simply the sum of the emissivities of its ordered component and its random part. We will show, instead, that a general theory can be developed, as a rather natural extension of the treatment for a uniform MF.

Let us consider now a MF $\boldsymbol{B} = \bar{\boldsymbol{B}} + \delta\boldsymbol{B}$, where $\bar{\boldsymbol{B}}$ is its average (which, without loss of generality, we assume to be directed along $\hat{y}$) while $\delta\boldsymbol{B}$ varies randomly according to an isotropic Gaussian distribution. Indeed, one may envisage an ample choice of statistical distributions for the random component. For instance, one could have assumed $\delta\boldsymbol{B}$ to be perpendicular to $\bar{\boldsymbol{B}}$. Our choice is motivated instead not only by an advantage for the computations but also because, with our recipe, we can treat in a continuous and homogeneous way both cases in which fluctuations are just a small perturbation and those in which they dominate, and that in all cases the observed emission depends uniquely on the properties of the projected MF. Instead, for instance, the prescription of purely transverse fluctuations would have led to the paradox that, in the limit of very large fluctuations, an energetically irrelevant $\bar{\boldsymbol{B}}$ would still play a leading role, determining the orientation of fluctuations. Another important constraint on the fluctuations is that they must be consistent with a vanishing divergence of the total MF. However, this constraint applies only to the spatial derivatives of $\delta\boldsymbol{B}$, while its one-point statistical distribution (as in our treatment) is not affected.

Then, the distribution of the projected components of the combined MF are

$$\mathcal{P}_x(B_x) = \frac{1}{\sqrt{2\pi}\sigma} \exp\left(-\frac{B_x^2}{2\sigma^2}\right) \tag{17}$$

and

$$\mathcal{P}_y(B_y) = \frac{1}{\sqrt{2\pi}\sigma} \exp\left(-\frac{(B_y - \bar{B})^2}{2\sigma^2}\right), \tag{18}$$

where σ is the standard deviation of the fluctuations, while the projected component $\bar{B}$ of the unperturbed MF is taken to be oriented along y. Note that, from now on, we will skip the index $\perp$ on both unperturbed MF and MF perturbations. In fact, without loss of generality, we will consider only the transverse MF components. By changing the element area from $\mathrm{d}B_x\,\mathrm{d}B_y$ to $\mathrm{d}B\,\mathrm{d}B_y$ and then

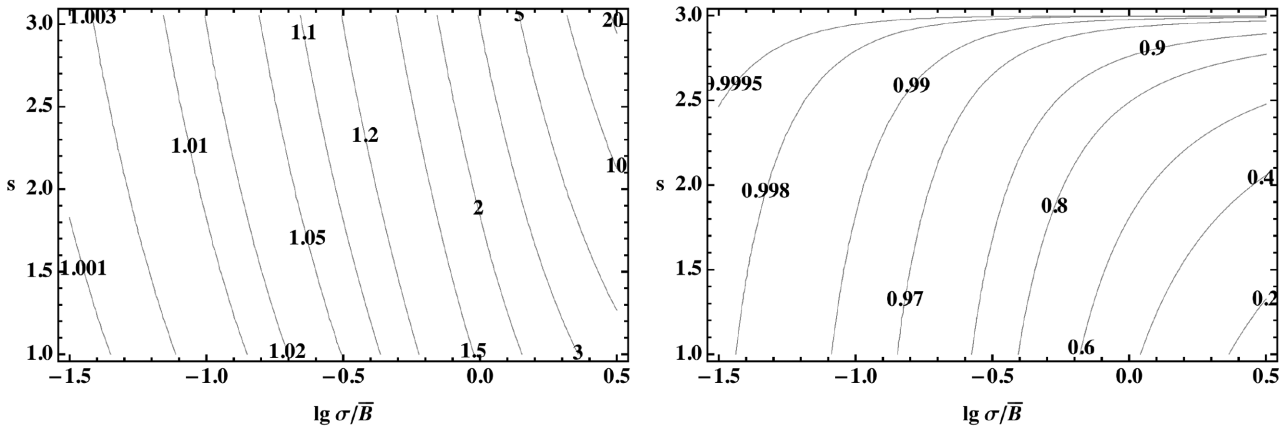

Figure 1. Maps of $\langle\mathcal{I}\rangle_{\rm PL}/\mathcal{I}_{\rm PL}$ (left) and $\langle\mathcal{Q}\rangle_{\rm PL}/\mathcal{Q}_{\rm PL}$ (right), as functions of $\sigma/\bar{B}$ and s, for when the random MF component is isotropic.

integrating over B_y we obtain

$$\begin{aligned}\mathcal{P}(B) &= \int_{-B}^{+B} \mathcal{P}_x(B_x)\mathcal{P}_y(B_y)\,2\,\left.\frac{\partial B_x}{\partial B}\right|_{B_y} \mathrm{d}B_y \\ &= \int_{-B}^{+B} \exp\left(-\frac{B^2-2B_y\bar{B}+\bar{B}^2}{2\sigma^2}\right)\frac{B\,\mathrm{d}B_y}{\pi\sigma^2\sqrt{B^2-B_y^2}} \\ &= I_0\left(\frac{B\,\bar{B}}{\sigma^2}\right)\exp\left(-\frac{B^2+\bar{B}^2}{2\sigma^2}\right)\frac{B}{\sigma^2}, \end{aligned} \tag{19}$$

with $I_n(z)$ being a modified Bessel function of the first kind (note that during that change of variable, a factor 2 has been introduced to keep track of the multiplicity in B_x).

The average Stokes parameters for a fluctuating MF can be obtained by averaging over the probability distribution of the MF fluctuations. For the total intensity $\mathcal{I}$, we then simply have

$$\begin{aligned}\langle\mathcal{I}\rangle &= \int_0^\infty \mathcal{I}\,\mathcal{P}(B)\,\mathrm{d}B \\ &= \int_0^\infty HF\left(\frac{2K}{B\gamma^2}\right) I_0\left(\frac{B\,\bar{B}}{\sigma^2}\right)\exp\left(-\frac{B^2+\bar{B}^2}{2\sigma^2}\right)\frac{B^2\,\mathrm{d}B}{\sigma^2}. \end{aligned} \tag{20}$$

As for the Stokes parameters Q and U, one must note that, while the average MF is oriented along y, this is not the case for the instantaneous MF, in which case these parameters (given above with respect to the orientation of the MF) must all be derotated to the y-axis, by using equations (8) and (9), before integration. We then obtain

$$\begin{aligned}\langle\mathcal{Q}\rangle &= \int HG\left(\frac{2K}{B\gamma^2}\right)\exp\left(-\frac{B^2-2B_y\bar{B}+\bar{B}^2}{2\sigma^2}\right) \\ &\quad\cdot\frac{\left(B^2-2B_y^2\right)\,\mathrm{d}B_y}{\pi\sigma^2\sqrt{B_y^2}}\mathrm{d}B \\ &= \int HG\left(\frac{2K}{B\gamma^2}\right) I_2\left(\frac{B\,\bar{B}}{\sigma^2}\right)\exp\left(-\frac{B^2+\bar{B}^2}{2\sigma^2}\right)\frac{B^2\mathrm{d}B}{\sigma^2}. \end{aligned} \tag{21}$$

$\langle\mathcal{U}\rangle = 0$ for symmetry reasons. All the above formulae refer to an ensemble of particles with a fixed Lorentz factor γ, while for a general energy distribution function, one should convolve the above expressions for $\langle\mathcal{I}\rangle$ and $\langle\mathcal{Q}\rangle$ by the particle distribution.

This convolution can be performed rather easily for a pure power-law energy distribution $n(\gamma) = A\gamma^{-s}$. In this case, by making use of the following identities:

$$\int_0^\infty x^\mu F(x)\,\mathrm{d}x = \frac{2^{\mu+1}}{\mu+2}\,\Gamma\left(\frac{\mu}{2}+\frac{7}{3}\right)\Gamma\left(\frac{\mu}{2}+\frac{2}{3}\right) \tag{22}$$

and

$$\int_0^\infty x^\mu G(x)\,\mathrm{d}x = 2^\mu\,\Gamma\left(\frac{\mu}{2}+\frac{4}{3}\right)\Gamma\left(\frac{\mu}{2}+\frac{2}{3}\right), \tag{23}$$

one gets

$$\begin{aligned}\langle\mathcal{I}\rangle_{\rm PL} &= \frac{s+7/3}{s+1}W_{\rm o}\sigma^{(s+1)/2}\int I_0\left(\frac{B\,\bar{B}}{\sigma^2}\right) \\ &\quad\cdot\exp\left(-\frac{B^2+\bar{B}^2}{2\sigma^2}\right)\frac{B^{(s+3)/2}\mathrm{d}B}{\sigma^{(s+5)/2}} \end{aligned} \tag{24}$$

and

$$\begin{aligned}\langle\mathcal{Q}\rangle_{\rm PL} &= W_{\rm o}\sigma^{(s+1)/2}\int I_2\left(\frac{B\,\bar{B}}{\sigma^2}\right) \\ &\quad\cdot\exp\left(-\frac{B^2+\bar{B}^2}{2\sigma^2}\right)\frac{B^{(s+3)/2}\mathrm{d}B}{\sigma^{(s+5)/2}}. \end{aligned} \tag{25}$$

The integrations can be performed in terms of special functions, giving

$$\begin{aligned}\langle\mathcal{I}\rangle_{\rm PL} &= \mathcal{I}_{\rm PL}\left\{\Gamma\left(\frac{5+s}{4}\right)\left(\frac{\bar{B}}{\sqrt{2}\sigma}\right)^{-(1+s)/2}\right. \\ &\quad\left.\cdot\,{}_1F_1\left(-\frac{1+s}{4},1,-\frac{\bar{B}^2}{2\sigma^2}\right)\right\} \end{aligned} \tag{26}$$

and

$$\begin{aligned}\langle\mathcal{Q}\rangle_{\rm PL} &= \mathcal{Q}_{\rm PL}\left\{\frac{1}{2}\Gamma\left(\frac{9+s}{4}\right)\left(\frac{\bar{B}}{\sqrt{2}\sigma}\right)^{(3-s)/2}\right. \\ &\quad\left.\cdot\,{}_1F_1\left(\frac{3-s}{4},3,-\frac{\bar{B}^2}{2\sigma^2}\right)\right\}, \end{aligned} \tag{27}$$

where ${}_1F_1(a, b, z)$ is the Kummer confluent hypergeometric function. Fig. 1 shows that both factors in braces approach unity for $\sigma/\bar{B}\to 0$ and the known results are recovered for a vanishing random component of MF. In the opposite limit, both hypergeometric factors approach unity, so that asymptotically

$$\langle\mathcal{I}\rangle_{\rm PL,asymp} = \frac{s+7/3}{s+1}\Gamma\left(\frac{5+s}{4}\right)W_{\rm o}\left(\sqrt{2}\sigma\right)^{(s+1)/2} \tag{28}$$

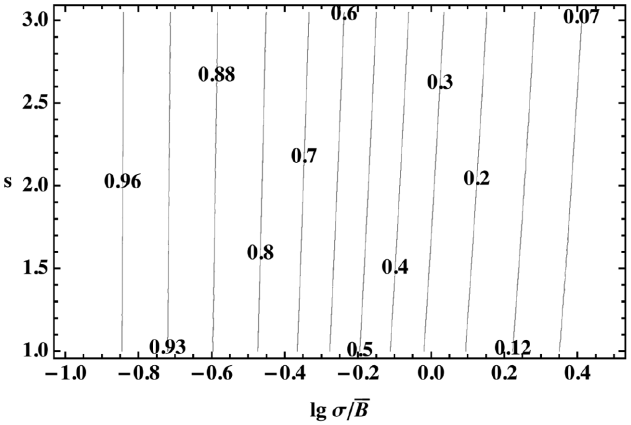

Figure 2. Map of $\Pi/\Pi_{\rm max}$ for isotropic fluctuations, where $\Pi_{\rm max}$ is for a uniform MF. Note how weakly $\Pi/\Pi_{\rm max}$ depends on s.

and

$$\langle \mathcal{Q} \rangle_{\rm PL,asymp} = \frac{1}{2}\Gamma\left(\frac{9+s}{4}\right) W_{\rm o} \bar{B}^2 \left(\sqrt{2}\sigma\right)^{(s-3)/2} \tag{29}$$

(cf. equations 13 and 14). This means that, for $\sigma \gg \bar{B}$, apart from a numerical factor, the asymptotic formula for $\langle \mathcal{I} \rangle_{\rm PL}$ is formally similar to $\mathcal{I}_{\rm PL}$, with $\sqrt{2}\sigma$ taking the place of the ordered MF, while the formula for $\langle \mathcal{Q} \rangle_{\rm PL}$ is asymptotically proportional to $\bar{B}^2\sigma^{(s-3)/2}$, leading to the asymptotic formula for the polarization fraction

$$\Pi_{\rm asymp} \simeq \frac{s+1}{s+7/3}\frac{5+s}{8}\frac{\bar{B}^2}{2\sigma^2} \tag{30}$$

from which one can easily see how the polarization fraction vanishes, in the limit of a large random MF component.

To conclude, the general formula for the polarization fraction becomes

$$\Pi = \Pi_{\rm max}\frac{(5+s)}{8}\frac{\bar{B}^2}{2\sigma^2}\frac{{}_1F_1\left((3-s)/4, 3, -\bar{B}^2/2\sigma^2\right)}{{}_1F_1\left(-(1+s)/4, 1, -\bar{B}^2/2\sigma^2\right)}. \tag{31}$$

The general behaviour of $\Pi/\Pi_{\rm max}$ is given in Fig. 2, showing that $\Pi/\Pi_{\rm max}$ is only weakly dependent on s.

2.3 An anisotropic random MF

A scenario somehow different from that outlined above is for efficient particle acceleration in a quasi-parallel shock (see e.g. Caprioli & Spitkovsky 2014a, and references therein). In this case, strong MF turbulent amplification takes place upstream of the shock front. This turbulent MF is roughly isotropic, as long as it keeps upstream, but the compression at the shock has the effect of enhancing the field components parallel to the shock front, leading to an anisotropic random MF component downstream. Under general conditions, this case is more complex than that outlined in the previous section, and does not allow an analytic solution. However, it becomes considerably simpler for a negligible original MF ($\bar{B} = 0$), a condition physically rather reasonable, whenever the MF experiences strong amplification.

Let us consider also in this case just the projected MF, and assume the following distributions for the two components:

$$\mathcal{P}_x(B_x) = \frac{1}{\sqrt{2\pi}\sigma_x}\exp\left(-\frac{B_x^2}{2\sigma_x^2}\right) \tag{32}$$

and

$$\mathcal{P}_y(B_y) = \frac{1}{\sqrt{2\pi}\sigma_y}\exp\left(-\frac{B_y^2}{2\sigma_y^2}\right), \tag{33}$$

where σ_x and σ_y are the standard deviations of the fluctuations along the two axes (here we also assume $\sigma_y > \sigma_x$, while the more general case can be obtained by a mere rotation of the axes). In an analogous way to the previous section,

$$\begin{aligned}\mathcal{P}(B) &= \int_{-B}^{+B}\exp\left(-\frac{B^2-B_y^2}{2\sigma_x^2}-\frac{B_y^2}{2\sigma_y^2}\right)\frac{B\,{\rm d}B_y}{\pi\sigma_x\sigma_y\sqrt{B^2-B_y^2}}\\ &= I_0\left(B^2\frac{\sigma_y^2-\sigma_x^2}{4\sigma_x^2\sigma_y^2}\right)\exp\left(-B^2\frac{\sigma_x^2+\sigma_y^2}{4\sigma_x^2\sigma_y^2}\right)\frac{B}{\sigma_x\sigma_y}.\end{aligned} \tag{34}$$

The average Stokes parameters can then be evaluated as

$$\begin{aligned}\langle \mathcal{I} \rangle &= \int_0^\infty HF\left(\frac{2K}{B\gamma^2}\right) I_0\left(B^2\frac{\sigma_y^2-\sigma_x^2}{4\sigma_x^2\sigma_y^2}\right)\\ &\cdot\exp\left(-B^2\frac{\sigma_x^2+\sigma_y^2}{4\sigma_x^2\sigma_y^2}\right)\frac{B^2{\rm d}B}{\sigma_x\sigma_y}\end{aligned} \tag{35}$$

and

$$\begin{aligned}\langle \mathcal{Q} \rangle &= \int_0^\infty HG\left(\frac{2K}{B\gamma^2}\right) I_1\left(B^2\frac{\sigma_y^2-\sigma_x^2}{4\sigma_x^2\sigma_y^2}\right)\\ &\cdot\exp\left(-B^2\frac{\sigma_x^2+\sigma_y^2}{4\sigma_x^2\sigma_y^2}\right)\frac{B^2{\rm d}B}{\sigma_x\sigma_y},\end{aligned} \tag{36}$$

while, again, $\langle \mathcal{U} \rangle = 0$ for symmetry reasons. These relations can be simplified, by introducing an effective dispersion and an asymmetry factor, defined as

$$\sigma_{\rm eff}^2 = \frac{2\sigma_x^2\sigma_y^2}{\sigma_x^2+\sigma_y^2}, \qquad f_{\rm an} = \frac{\sigma_y^2-\sigma_x^2}{\sigma_x^2+\sigma_y^2}. \tag{37}$$

Equations (35) and (36) can then be rewritten as

$$\begin{aligned}\langle \mathcal{I} \rangle &= \int_0^\infty HF\left(\frac{2K}{B\gamma^2}\right) I_0\left(f_{\rm an}\frac{B^2}{2\sigma_{\rm eff}^2}\right)\\ &\cdot\exp\left(-\frac{B^2}{2\sigma_{\rm eff}^2}\right)\frac{\sqrt{1-f_{\rm an}^2}B^2{\rm d}B}{\sigma_{\rm eff}^2}\end{aligned} \tag{38}$$

and

$$\begin{aligned}\langle \mathcal{Q} \rangle &= \int_0^\infty HG\left(\frac{2K}{B\gamma^2}\right) I_1\left(f_{\rm an}\frac{B^2}{2\sigma_{\rm eff}^2}\right)\\ &\cdot\exp\left(-\frac{B^2}{2\sigma_{\rm eff}^2}\right)\frac{\sqrt{1-f_{\rm an}^2}B^2{\rm d}B}{\sigma_{\rm eff}^2}.\end{aligned} \tag{39}$$

The convolution with a pure power-law energy distribution finally leads to

$$\begin{aligned}\langle \mathcal{I} \rangle_{\rm PL} &= \left(\frac{s+7/3}{s+1}W_{\rm o}\left(2\sigma_{\rm eff}^2\right)^{(s+1)/4}\right)\\ &\cdot\left\{\sqrt{1-f_{\rm an}^2}\,\Gamma\left(\frac{5+s}{4}\right){}_2F_1\left(\frac{5+s}{8}, \frac{9+s}{8}, 1, f_{\rm an}^2\right)\right\}\end{aligned} \tag{40}$$

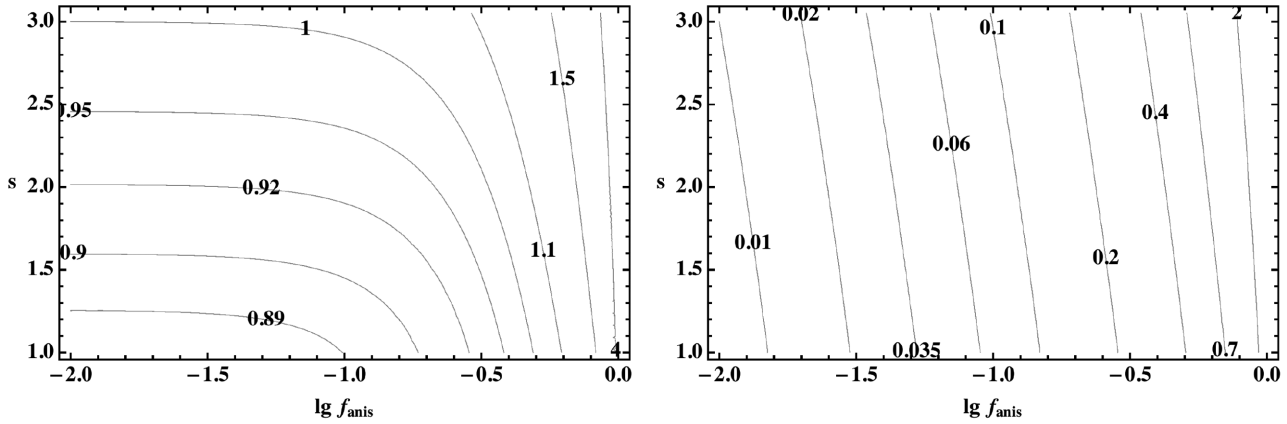

Figure 3. Maps of $\langle\mathcal{I}\rangle_{PL}/\mathcal{I}_{PL}$ and $\langle\mathcal{Q}\rangle_{PL}/\mathcal{Q}_{PL}$ for anisotropic fluctuations and a vanishing ordered MF component, as functions of f_{an} and s.

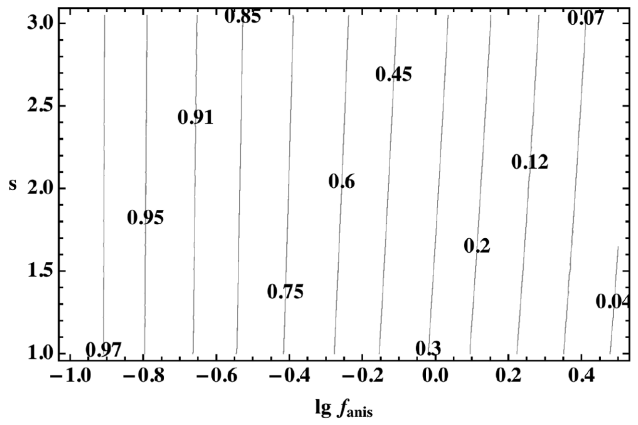

Figure 4. Map of Π/Π_{max} for anisotropic fluctuations and a vanishing ordered MF component. Note that also in this case Π/Π_{max} depends very weakly on s.

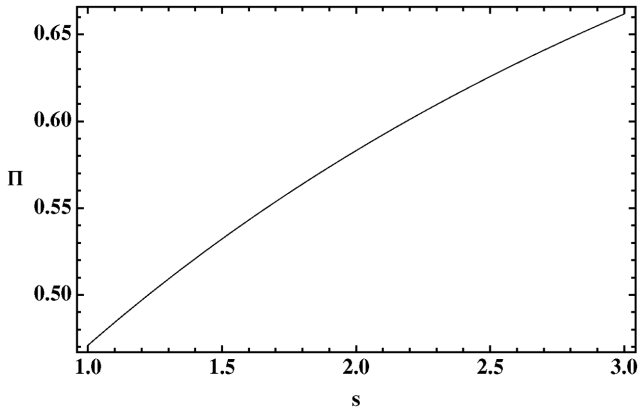

Figure 5. Polarization fraction as a function of s for a shock compression of an originally isotropic random MF.

and

$$\langle\mathcal{Q}\rangle_{PL} = \left(W_o\left(2\sigma_{eff}^2\right)^{(s+1)/4}\right) \cdot\left\{\frac{f_{an}}{2}\sqrt{1-f_{an}^2}\,\Gamma\left(\frac{9+s}{4}\right){}_2F_1 \times\left(\frac{9+s}{8},\frac{13+s}{8},2,f_{an}^2\right)\right\}, \tag{41}$$

where ${}_2F_1(a, b, c, z)$ is the Gauss hypergeometric function (see Fig. 3). Note in the above two equations, the formal similarity of the leading factors and equations (13) and (14), with $\sqrt{2}\sigma_{eff}$ taking the place of $B_\perp$. The general formula for the polarization fraction then becomes

$$\Pi = \Pi_{max}\left\{\frac{(5+s)f_{an}\;{}_2F_1\left((9+s)/8,(13+s)/8,2,f_{an}^2\right)}{8\;{}_2F_1\left((5+s)/8,(9+s)/8,1,f_{an}^2\right)}\right\}. \tag{42}$$

The ratio Π/Π_{max}, as shown in Fig. 4, is only weakly dependent on s. In the limit of $\sigma_x \simeq \sigma_y$ [i.e. $\sigma = (\sigma_x + \sigma_y)/2$ and $\delta\sigma = \sigma_y - \sigma_x \ll \sigma$]:

$$\sigma_{eff} \simeq \sigma - \frac{3\,\delta\sigma^2}{8\sigma}, \qquad f_{an} \simeq \frac{\delta\sigma}{\sigma}, \tag{43}$$

and then the factors in braces in equations (40) and (41) respectively approach

$$\Gamma\left(\frac{5+s}{4}\right) \qquad \text{and} \qquad \frac{5+s}{4}\,\Gamma\left(\frac{5+s}{4}\right)\frac{f_{an}}{2}. \tag{44}$$

This leads to a small polarization fraction:

$$\Pi = \frac{s+1}{s+7/3}\,\frac{5+s}{8}\,f_{an}. \tag{45}$$

Instead, in the limit $\sigma_y \ll \sigma_x$:

$$\sigma_{eff} \simeq \sqrt{2}\sigma_y, \qquad f_{an} \simeq 1 - \frac{2\sigma_y^2}{\sigma_x^2}, \tag{46}$$

and in this case both factors within braces in equations (40) and (41) approach

$$\Gamma\left(\frac{3+s}{4}\right)\frac{(1-f_{an})^{-(1+s)/4}}{\sqrt{\pi}}, \tag{47}$$

therefore, leading, as expected, to the same limit value of the polarization fraction as for a fully ordered MF.

The above results can be readily applied to estimate the polarization induced by a shock compression. If the projected shock velocity is along the x-axis, in the downstream σ_x would be equal to σ in the upstream, while σ_y would be enhanced by a factor κ (where κ is the shock compression ratio). For a strong shock with $\kappa = 4$, then f_{an} would be equal to 15/17. The related polarization fraction, evaluated from equation (42), is shown in Fig. 5. Note that in this

case the downstream emission still exhibits a strong polarization, much stronger than typically measured in typical shell-like SNRs.

2.4 Mono-energetic electron distribution

We have shown how, for a power-law energy distribution of the electrons, one may obtain in a rather elegant way analytic formulae for the polarized emission that resembles the classical formulae for a fully ordered MF.

Unfortunately, for a general particle energy distribution, the situation is much more complex, and there is no guarantee of the existence of analytic solutions. Just to give the feel of the kind of additional problems arising in the general case, let us consider here the total intensity ($\langle\mathcal{I}\rangle_\gamma$) for a mono-energetic distribution of particles. This requires one to solve equation (20) for a fixed γ value. In spite of the expected simplicity of this problem, we have not found any analytic solution to it except for the two limiting cases, namely a fully ordered and a completely random MF.

The former case is simply proportional to the emitted spectrum from a single particle, equation (8). The latter case, instead, is obtained by evaluating equation (20) in the limit $\bar{B} = 0$. Using equation (3) for the definition of $F(x)$, and inverting the integration order, one may reduce equation (20) to

$$\begin{aligned}\langle\mathcal{I}\rangle &= H\sigma \int_0^\infty K_{5/3}(z)\frac{\omega}{\omega_{c,\sigma}}\exp\left(-\frac{\omega^2}{\omega_{c,\sigma}^2}\frac{1}{2z^2}\right)\mathrm{d}z \\ &= H\sigma\frac{\pi}{\sqrt{3}}\left(\frac{\omega}{\omega_{c,\sigma}}+\frac{4}{3}\frac{\omega^{1/3}}{\omega_{c,\sigma}^{1/3}}\right)\exp\left(-\frac{3}{2}\frac{\omega^{2/3}}{\omega_{c,\sigma}^{2/3}}\right) \\ &\hat{=} H\sigma F_\sigma(\omega/\omega_{c,\sigma}),\end{aligned} \tag{48}$$

where we have introduced the quantities F_σ (defined above), and

$$\omega_{c,\sigma} = \frac{3}{2}\frac{e\,\sigma}{m_e c}\gamma^2, \tag{49}$$

to obtain a formula that formally resembles equation (8). Fig. 6 compares $F(x)$ and $F_\sigma(\sqrt{2}x)/\sqrt{2}$ (where the $\sqrt{2}$ factors arise since in the completely random case, the effective MF strength would be equal to $\sqrt{2}\sigma$). The present analysis is in a sense similar to that in Pohl, Wilhelm & Telezhinsky (2015). The main differences are that that paper assumes a 1D Gaussian distribution for the MF values and an approximation of $F(x)$, while here we use a 2D one, which we think is more correct, and the exact $F(x)$ function. Interestingly, our approach luckily allows an exact solution.

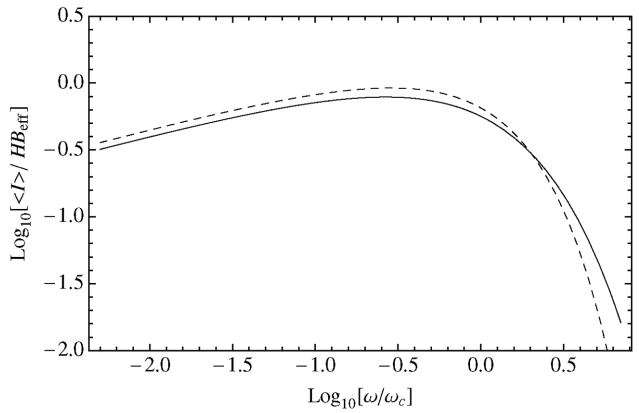

Figure 6. Comparison of the spectral profile of the synchrotron emissivity from a mono-energetic particle distribution, both for a completely ordered MF (dashed line) and a fully random MF (solid line). $B_{\rm eff}$ indicates the effective MF for each case, namely $\bar{B}$ in the former case and $\sqrt{2}\sigma$ in the latter.

However, no analytic solution is known for cases intermediate between a fully ordered and a fully random field. This issue, which is also preliminary to any further generalization to particle energy distributions different from the pure power-law one (the case thoroughly treated in the present work), will need a separate treatment.

3 MODELLING SHELL-TYPE SNRS

To apply the formulae derived in the previous section and to synthesize the emission and polarization maps for shell-like SNRs, we need to introduce SNR models on which to integrate the contribution of all volume elements along the lines of sight. In the most general case, the number of parameters would unfortunately be so large as to hinder any extensive investigation in the parameter space.

For this reason, in the rest of this paper we will limit our discussion to a thin-layer model of a spherical shell-type SNR. According to this approximation, at each position of the map, the observed emission originates from two (geometrically thin) limbs, at a physical distance $R_{\rm s}$ from the SNR centre. Moreover, we assume that we can substitute the actual profiles of all physical quantities (like the density of the thermal gas, that of the relativistic particles, as well as the MF direction and strength) with their average values. As we shall see, also this very simplified approximation may lead to rather complex and various phenomenologies. In a forthcoming paper, we shall release this assumption, and discuss the validity and limits of the thin-layer approximation.

In the rest of this section we will describe in more detail the various elements of this model.

3.1 Physical and projected coordinates

A very important although just geometrical task is to convert specific elements in the SNR from and to points on the observed map, and in this section we present some relations that make this conversion easier.

Let $\{r, \theta, \varphi\}$ be the spherical coordinates in a reference system oriented with respect to a given axis that we will identify with the SNR axis. To simplify the modelling further, we also assume that the SNR is axially symmetric, namely there is no explicit dependence on φ of the SNR physical quantities. Moreover, as before, let $\{x, y\}$ be the coordinates of the map and z that along the line of sight.

Let us also define ϱ and Θ as the projected radial and angular coordinates, and $\phi_{\rm o}$ as the angle (aspect angle) by which the SNR axis is tilted with respect to the line of sight. The projection of the SNR axis can be assumed, without loss of generality, to lie along the x direction. A preliminary step is to set the conversion between the two sets of coordinates. Under the above assumptions, the map coordinates read

$$x = \varrho\cos\Theta = r\,(\cos\phi_{\rm o}\sin\theta\cos\varphi + \sin\phi_{\rm o}\cos\theta) \tag{50}$$

and

$$y = \varrho\sin\Theta = r\ \sin\theta\sin\varphi, \tag{51}$$

while the line of sight coordinate

$$z = r\,(\cos\phi_{\rm o}\cos\theta - \sin\phi_{\rm o}\sin\theta\cos\varphi)\,. \tag{52}$$

Using equations (50) and (51), one can derive

$$\cos\varphi = \frac{\tilde{\varrho}\cos\Theta - \sin\phi_{\rm o}\cos\theta}{\cos\phi_{\rm o}\sin\theta} \tag{53}$$

and

$$\sin\varphi = \frac{\tilde{\varrho}\sin\Theta}{\sin\theta}, \tag{54}$$

where $\tilde{\varrho} = \varrho/r$, which is always less than unity. Note that, if we consider a spherical shell, the tilt angle (τ) of an element of surface would be such that $\sin\tau = \tilde{\varrho}$.

Equations (53) and (54) can be combined to give

$$\cos\theta = \tilde{\varrho}\sin\phi_{\rm o}\cos\Theta \pm \cos\phi_{\rm o}\sqrt{1-\tilde{\varrho}^2}, \tag{55}$$

the two solutions referring respectively to the nearer and further limbs of the sphere of radius r, intercepted by the line of sight.

3.2 MF geometry

Probably the most natural geometry for the ordered MF component is that based on the idea that the SNR expands in an ambient medium with a pre-existing uniform ambient MF $B_{\rm amb}$, and that the MF structure inside the SNR itself is a direct consequence of compression. We also assume that the morphology of the SNR emission is affected by this MF geometry, and in particular that the SNR symmetry axis is aligned with the ambient MF direction.

Within the thin-layer approach, all MF lines are asymptotically aligned along the meridians. Therefore, in the SNR reference frame, the magnetic unit vector is

$$\hat{\boldsymbol{B}} = \{-\cos\theta\cos\varphi, -\cos\theta\sin\varphi, \sin\theta\}, \tag{56}$$

or with opposite sign, depending on the MF orientation (anyway, this orientation does not affect in any way the values of the Stokes parameters). The projection of this unit vector on the x–y plane is then

$$\left\{\frac{\sin\phi_{\rm o} - \tilde{\varrho}\cos\Theta\cos\theta}{\sin\theta}, -\frac{\tilde{\varrho}\sin\Theta\cos\theta}{\sin\theta}\right\}, \tag{57}$$

while the magnetic pitch angle α is

$$\cos\alpha = \frac{\sin\theta^2 - \sin\phi_{\rm o}^2 + \tilde{\varrho}\cos\Theta\cos\theta\sin\phi_{\rm o}}{\cos\phi_{\rm o}\sin\theta}. \tag{58}$$

As for the strength of the ordered MF, flux conservation leads to

$$\bar{B} = \frac{\sin\theta\, B_{\rm amb}}{1-(1-w(\theta)/R_{\rm s})^2} \simeq \frac{\sin\theta\, B_{\rm amb}}{2w(\theta)/R_{\rm s}}, \tag{59}$$

where $w(\theta)$ is the layer thickness, the thin-layer approximation requiring $w(\theta) \ll R_{\rm s}$ at all θ. This results in an artificially large B, but it does not affect the patterns on the polarization maps.

Also the densities of the thermal and relativistic particle components will depend on the layer thickness. Mass conservation implies:

$$\rho = \frac{\rho_{\rm amb}}{1-(1-w(\theta)/R_{\rm s})^3} \simeq \frac{\rho_{\rm amb}}{3\,w(\theta)/R_{\rm s}}. \tag{60}$$

Let us also assume that the relativistic component is frozen in the MF and evolves adiabatically (the Lorentz factors then evolving as $\gamma \propto \rho^{1/3}$). In this case, the normalization factor A, as defined in equation (12), is

$$A = A_{\rm s}\left(\frac{\rho}{\rho_{\rm s}}\right)^{1+(s-1)/3} = A_{\rm s}(\theta)\left(\frac{3w(\theta)}{4R_{\rm s}}\right)^{(s+2)/3}. \tag{61}$$

The quantity $A_{\rm s}(\theta)$, namely its value right downstream of the shock, is generally unknown. Let us assume here that, for simplicity, both $w(\theta)$ and $A_{\rm s}(\theta)$ are constant. These values are not important here, because in the rest of the paper we will concentrate on the form factors, and we will present only normalized emission maps. Let us add that, as shown by equations (13)–(15), the synchrotron emissivity at a given frequency ω is proportional to $AB_{\perp}^{(s+1)/2}$. Therefore, there is a degeneracy between the layer thickness, the normalization of the energy distribution of particles and the MF strength [to the power $(s+1)/2$], in the sense that if we scale any of them by a given factor, the resulting emissivity will be scaled by the same factor, leaving completely unchanged the patterns on the various maps.

Another MF geometry, suggested by radio polarization maps of younger SNRs (Milne 1987), is the radial one, namely

$$\hat{\boldsymbol{B}} = \{\sin\theta\cos\varphi, \sin\theta\sin\varphi, \cos\theta\}. \tag{62}$$

Of course, this does not imply the (quite unphysical) assumption of a magnetic monopole. Since the polarization properties of the synchrotron emission do not depend on the MF orientation, one could imagine a mixture of inward- and outward-oriented radial MF lines. Unlike the previous case, now there is no obvious recipe for the dependence of the ordered MF strength on the position, so we will have to choose it a priori (see the two cases discussed in Section 5).

3.3 Faraday rotation

The Stokes parameters projected on to the plane of the sky can be obtained by integration of the local values along the line of sight. However, for the two Stokes parameters related to linear polarization, one should also take into account the FR, a propagation effect that produces a rotation (by an angle β) of the polarization plane, according to the formula

$$\beta(z_1, z_2) = \frac{e^3\lambda^2}{2\pi m_{\rm e}^2 c^4}\int_{z_1}^{z_2} n(z')B_z(z')\,{\rm d}z', \tag{63}$$

with n being the local plasma electron density, $\lambda = 2\pi c/\omega$ the radiation wavelength, and z_2, z_1 two given positions along the line of sight (of which z_2 is the closer to the observer). By defining the rotation measure as

$${\rm RM}(z_1, z_2) = \frac{e^3}{2\pi m_{\rm e}^2 c^4}\int_{z_1}^{z_2} n(z')B_z(z')\,{\rm d}z', \tag{64}$$

one can simply write $\beta = {\rm RM}\,\lambda^2$. To simplify the notation in some points, we will also use ${\rm RM}(z) = {\rm RM}(z, z_{\rm obs})$ (where $z_{\rm obs}$ is at the observer's location). This formula for the FR is linear in B, which means that only the ordered MF matters, while the effect of fluctuations averages to zero.

It is, however, necessary to distinguish between foreground FR (that produced by the medium between the SNR and the observer) and internal FR (that produced inside the SNR itself). The effect of a foreground medium on the observed Stokes parameters (of course, only Q and U are affected) is the following

$$Q = \cos(2\beta)Q_{\rm i} - \sin(2\beta)U_{\rm i} \tag{65}$$

and

$$U = \sin(2\beta)Q_{\rm i} + \cos(2\beta)U_{\rm i}, \tag{66}$$

where $Q_{\rm i}$ and $U_{\rm i}$ indicate the intrinsic Stokes parameters, namely in the absence of FR, as is the case for $\lambda \to 0$. β is the angle of rotation accumulated between the source boundary closest to the observer and $z_{\rm obs}$. Note that the above formulae are not only valid for describing the effect of the interstellar medium in front of the SNR, but also that of the SNR front-side limb with respect to the emission from the rear-side limb.

Instead, the effect of the internal FR on the observed polarization is more complex, since different rotation measures apply to the

radiation emitted in different layers, so that a double integral is required to evaluate its overall effect.

As will be shown better below, a more general relation between the intrinsic and observed Stokes parameters is given by

$$Q = f_{\rm obs}\left(\cos(2{\rm RM}_{\rm obs}\lambda^2)Q_{\rm i} - \sin(2{\rm RM}_{\rm obs}\lambda^2)U_{\rm i}\right) \tag{67}$$

and

$$U = f_{\rm obs}\left(\sin(2{\rm RM}_{\rm obs}\lambda^2)Q_{\rm i} + \cos(2{\rm RM}_{\rm obs}\lambda^2)U_{\rm i}\right), \tag{68}$$

which allow us to define what we intend by the observed Faraday depolarization factor ($f_{\rm obs}$) and RM (${\rm RM}_{\rm obs}$). Only for a purely foreground FR do we have $f_{\rm obs} = 1$ and ${\rm RM}_{\rm obs}$ equal to the quantity described by equation (64). In the general case, both $f_{\rm obs}$ and ${\rm RM}_{\rm obs}$ will depend on λ.

Finally, note that, while the FR due to a foreground medium could be completely corrected in the post-processing phase (provided that the radio data have a sufficiently narrow bandwidth), no such correction could be applied for internal FR, since the intrinsic depolarization is irreversible.

3.4 Observed polarization

Before proceeding with the derivation of the observed Stokes parameters, let us draw the general equations that show how they are obtained, by integrating along the line of sight, and also accounting for the FR effect:

$$\begin{cases} I = \int_{z_1}^{z_2} \mathcal{I}(z'){\rm d}z', \\ Q = \int_{z_1}^{z_2} \Big(\cos\left(2\beta(z_1,z')\right)\mathcal{Q}(z') \\ \qquad\qquad - \sin\left(2\beta(z_1,z')\right)\mathcal{U}(z')\Big){\rm d}z', \\ U = \int_{z_1}^{z_2} \Big(\sin\left(2\beta(z_1,z')\right)\mathcal{Q}(z') \\ \qquad\qquad + \cos\left(2\beta(z_1,z')\right)\mathcal{U}(z')\Big){\rm d}z'. \end{cases} \tag{69}$$

The polarization fraction can be then derived as

$$\Pi = \frac{\sqrt{Q^2+U^2}}{I}. \tag{70}$$

The angle

$$\Psi = \frac{1}{2}\arctan\left(\frac{U}{Q}\right) \tag{71}$$

is orthogonal to the polarization angle, and gives the average orientation of the observed MF. Namely we have

$$B_x = B\cos\Psi, \qquad B_y = B\sin\Psi. \tag{72}$$

3.5 Single-layer case

The problem simplifies considerably within the thin-layer approximation, namely under the assumption that nB_z, as well as the specific $\mathcal{Q}$ and $\mathcal{U}$ values, are constant across the shell. In this case, since

$$\frac{{\rm d}\beta}{{\rm d}z'} = \frac{e^3\lambda^2}{2\pi m_{\rm e}^2 c^4} n B_z \tag{73}$$

is constant, the integration along a layer ($z_1 = 0$, $z_2 = z$) leads to the following relations:

$$\int_0^z \sin\left(2\frac{{\rm d}\beta}{{\rm d}z'}z'\right){\rm d}z' = z\frac{\sin\beta}{\beta}\sin\beta \tag{74}$$

and

$$\int_0^z \cos\left(2\frac{{\rm d}\beta}{{\rm d}z'}z'\right){\rm d}z' = z\frac{\sin\beta}{\beta}\cos\beta. \tag{75}$$

In addition, we readily have:

$$z\mathcal{Q} = Q_{\rm i}, \qquad z\mathcal{U} = U_{\rm i}. \tag{76}$$

Then combining all together, we finally get

$$Q = \frac{\sin(\beta)}{\beta}(\cos(\beta)Q_{\rm i} - \sin(\beta)U_{\rm i}) \tag{77}$$

and

$$U = \frac{\sin(\beta)}{\beta}(\sin(\beta)Q_{\rm i} + \cos(\beta)U_{\rm i}). \tag{78}$$

Namely, the amount of rotation is half of that for a foreground layer, while, unlike a foreground FR, which turns out to be a mere rotation of the polarization plane, now the observed polarization fraction is lower than the intrinsic one. In fact,

$$\sqrt{Q^2+U^2} = \left|\frac{\sin(\beta)}{\beta}\right|\sqrt{Q_{\rm i}^2+U_{\rm i}^2}. \tag{79}$$

3.6 Two-layer combination

For a thin-shell SNR, in each projected position we see the combination of the effects of two layers, each of them subject to internal FR, and in addition the front-side layer Faraday rotating the polarized emission from the rear-side one (in the following, we will label the front and rear limb quantities as 'f' and 'r', respectively). We then have

$$\begin{aligned} Q = {} & \frac{\sin\left({\rm RM}_{\rm f}\lambda^2\right)}{{\rm RM}_{\rm f}\lambda^2}\left(\cos\left({\rm RM}_{\rm f}\lambda^2\right)Q_{\rm f} - \sin\left({\rm RM}_{\rm f}\lambda^2\right)U_{\rm f}\right) \\ & + \frac{\sin\left({\rm RM}_{\rm r}\lambda^2\right)}{{\rm RM}_{\rm r}\lambda^2}\left(\cos\left({\rm RM}_{\rm x}\lambda^2\right)Q_{\rm r} - \sin\left({\rm RM}_{\rm x}\lambda^2\right)U_{\rm r}\right) \end{aligned} \tag{80}$$

and

$$\begin{aligned} U = {} & \frac{\sin\left({\rm RM}_{\rm f}\lambda^2\right)}{{\rm RM}_{\rm f}\lambda^2}\left(\sin\left({\rm RM}_{\rm f}\lambda^2\right)Q_{\rm f} + \cos\left({\rm RM}_{\rm f}\lambda^2\right)U_{\rm f}\right) \\ & + \frac{\sin({\rm RM}_{\rm r}\lambda^2)}{{\rm RM}_{\rm r}\lambda^2}\left(\sin({\rm RM}_{\rm x}\lambda^2)Q_{\rm r} + \cos\left({\rm RM}_{\rm x}\lambda^2\right)U_{\rm r}\right), \end{aligned} \tag{81}$$

where ${\rm RM}_{\rm x} = 2{\rm RM}_{\rm f} + {\rm RM}_{\rm r}$.

Even in the simplified case of two homogeneous thin layers, the formulae for $f_{\rm obs}$ and ${\rm RM}_{\rm obs}$ (as defined by equations 67 and 68) turn out to be rather complex. For this reason, we consider here the limit for small rotations, namely for small enough λ values, getting

$$\begin{aligned} f_{\rm obs} &= 1 - \frac{QU_{\rm m}{\rm RM}_{\rm t}}{\left(Q_{\rm i}^2+U_{\rm i}^2\right)}\lambda^2 + \mathcal{O}(\lambda^4) \\ &= 1 - f_{\rm obs,2}\lambda^2 + \mathcal{O}(\lambda^4) \end{aligned} \tag{82}$$

and

$$\begin{aligned} {\rm RM}_{\rm obs} = {} & \left(\frac{{\rm RM}_{\rm f}}{2} + \frac{QU_{\rm p}{\rm RM}_{\rm t}}{2\left(Q_{\rm i}^2+U_{\rm i}^2\right)}\right) \\ & + QU_{\rm m}\left(\frac{{\rm RM}_{\rm t}{\rm RM}_{\rm x}}{6\left(Q_{\rm i}^2+U_{\rm i}^2\right)} - \frac{QU_{\rm p}{\rm RM}_{\rm t}^2}{2(Q_{\rm i}^2+U_{\rm i}^2)^2}\right)\lambda^2 + \mathcal{O}\left(\lambda^4\right) \\ = {} & {\rm RM}_{\rm obs,0} + {\rm RM}_{\rm obs,2}\lambda^2 + \mathcal{O}\left(\lambda^4\right), \end{aligned} \tag{83}$$

where $QU_{\rm m} = Q_{\rm f}U_{\rm r} - Q_{\rm r}U_{\rm f}$, $QU_{\rm p} = Q_{\rm i}Q_{\rm r} + U_{\rm i}U_{\rm r}$, ${\rm RM}_{\rm t} = {\rm RM}_{\rm f} + {\rm RM}_{\rm r}$, $Q_{\rm i} = Q_{\rm f} + Q_{\rm r}$ and $U_{\rm i} = U_{\rm f} + U_{\rm r}$. Note that the quantity $f_{\rm obs}$, previously dubbed the depolarization factor, does not always lead to a decreased polarization level. In its series expansion, it depends on the sign of the coefficient of λ^2. This means that under some circumstances, the differential FR may have a constructive effect.

At least in principle, comparing polarizations measured at various wavelengths, including longer ones, would allow one to measure more coefficients of the power expansions with λ of both $\mathrm{RM_{obs}}$ and $f_{\rm obs}$, then allowing one to get further information on the MF structure. This is unfortunately a difficult observational task at the present time, but it should become feasible with the advent of larger radio telescopes operating at low-frequency radio wavelengths (like LOFAR and SKA).

3.7 A generalized momentum treatment

Releasing the thin-layer assumption, the treatment of the internal FR becomes considerably more complex, since the calculation of the observed Stokes parameters requires the explicit calculation of a double integral for each projected point. A complete solution of the inverse problem, namely how to derive from the observations the 3D structure of the density and MF, looks then essentially hopeless. However, in an analogous way to that shown in the previous section, some relations can be derived as power-law expansions, in the limit of wavelengths.

The observed Stokes parameters read

$$Q = \int \cos\left(2\mathrm{RM}(z)\lambda^2\right)\mathcal{Q}(z) - \sin\left(2\mathrm{RM}(z)\lambda^2\right)\mathcal{U}(z)\,\mathrm{d}z \tag{84}$$

and

$$U = \int \sin\left(2\mathrm{RM}(z)\lambda^2\right)\mathcal{Q}(z) + \cos\left(2\mathrm{RM}(z)\lambda^2\right)\mathcal{U}(z)\,\mathrm{d}z. \tag{85}$$

Let us introduce the quantities

$$Q_{\mathrm{i},n} = \int_0^\infty \mathcal{Q}(z)\mathrm{RM}(z)^n\,\mathrm{d}z \tag{86}$$

and

$$U_{\mathrm{i},n} = \int_0^\infty \mathcal{U}(z)\mathrm{RM}(z)^n\,\mathrm{d}z \tag{87}$$

(in the following, for $Q_{\mathrm{i},0}$ and $U_{\mathrm{i},0}$, we shall simply use $Q_{\rm i}$ and $U_{\rm i}$, respectively). It can be shown that the power expansions of both the observed depolarization $f_{\rm obs}$ and the rotation measure $\mathrm{RM_{obs}}$ can be expressed as fractions whose numerator is a polynomial of these I quantities, while the denominator is a power of $\left(Q_{\rm i}^2 + U_{\rm i}^2\right)$. We present here the expansions equivalent to those shown by equations (82) and (83) for the thin-layer case:

$$f_{\rm obs} = 1 - \frac{2(Q_{\rm i}U_{\mathrm{i},1} - U_{\rm i}Q_{\mathrm{i},1})}{(Q_{\rm i}^2 + U_{\rm i}^2)}\lambda^2 + \mathcal{O}\left(\lambda^4\right) \tag{88}$$

and

$$\mathrm{RM_{obs}} = \frac{Q_{\rm i}Q_{\mathrm{i},1} + U_{\rm i}U_{\mathrm{i},1}}{\left(Q_{\rm i}^2 + U_{\rm i}^2\right)} + \left(\frac{U_{\rm i}Q_{\mathrm{i},2} - Q_{\rm i}U_{\mathrm{i},2}}{\left(Q_{\rm i}^2 + U_{\rm i}^2\right)} + \frac{2\left(\left(Q_{\rm i}^2 - U_{\rm i}^2\right)Q_{\mathrm{i},1}U_{\mathrm{i},1} - Q_{\rm i}U_{\rm i}(Q_{\mathrm{i},1}^2 - U_{\mathrm{i},1}^2)\right)}{\left(Q_{\rm i}^2 + U_{\rm i}^2\right)^2}\right)\lambda^2 + \mathcal{O}\left(\lambda^4\right). \tag{89}$$

Equations (82) and (83) are indeed recovered, by substituting

$$Q_{\mathrm{i},1} = Q_{\rm r}\mathrm{RM_f} + \frac{Q_{\rm f}\mathrm{RM_f} + Q_{\rm r}\mathrm{RM_r}}{2}, \tag{90}$$

$$U_{\mathrm{i},1} = U_{\rm r}\mathrm{RM_f} + \frac{U_{\rm f}\mathrm{RM_f} + U_{\rm r}\mathrm{RM_r}}{2}, \tag{91}$$

$$Q_{\mathrm{i},2} = Q_{\rm r}\mathrm{RM_f^2} + \frac{Q_{\rm r}\mathrm{RM_f}\mathrm{RM_r}}{2} + \frac{Q_{\rm f}\mathrm{RM_f^2} + Q_{\rm r}\mathrm{RM_r^2}}{3} \tag{92}$$

and

$$U_{\mathrm{i},2} = U_{\rm r}\mathrm{RM_f^2} + \frac{U_{\rm r}\mathrm{RM_f}\mathrm{RM_r}}{2} + \frac{U_{\rm f}\mathrm{RM_f^2} + U_{\rm r}\mathrm{RM_r^2}}{3}. \tag{93}$$

Here is a list of general conclusions arising from this analysis (and that in some respects, confirms what was already found from the thin-layer approximated analysis):

(i) Unlike what happens when the FR is just due to foreground medium, the internal FR does not simply scale with λ^2.

(ii) While foreground FR does not cause depolarization (apart from that produced by the finite spectral width of the telescope), internal FR necessarily involves some change in the polarization level, which, depending on the case, may lead to depolarization or to an increase of the polarization fraction.

(iii) The momentum analysis can in principle provide an infinite number of observational constraints, which correspond to the various orders of the power expansion in λ of equations (88) and (89). Moreover, $Q \to Q_{\rm i}$ and $U \to U_{\rm i}$ for $\lambda \to 0$.

(iv) Unfortunately, the number of relations is not sufficient to derive $\mathcal{Q}(z)$, $\mathcal{U}(z)$ and $\mathrm{RM}(z)$ independently (but just two of them, given the third). Therefore, some a priori conditions on the MF and the emissivity must be given.

4 THIN-LAYER MODELS OF SNRS

In this section, we present and discuss some SNR models generated using the thin-layer approach described above. It is not our intention, at this stage, to model any individual SNR, also because real maps typically show patterns at smaller scales, which will not be considered here. Our present aim is just that of outlining some general trends, to give a better insight of the importance of the various parameters. For all models presented below, we have used a shell thickness 10^{-2} times its radius, and a power-law particle energy distribution with $s = 2$ (corresponding to a radio spectral index of 0.5, close to what is usually measured in SNRs). The exact value of the thickness (w, here taken to be constant), provided it is much smaller than $R_{\rm s}$, does not affect considerably the pattern of the emission maps, but just their flux normalization.

Notice that all maps of surface brightness presented below are normalized to

$$W_{\rm o}B_{\rm o}^{(s+1)/2}w, \tag{94}$$

where the quantities $W_{\rm o}$ and $B_{\rm o}$ are their respective maximum values within the shell, for instance, the equatorial value (namely that at $\theta = \pi/2$) for a meridional MF like that defined above. In the following maps (except when stated differently), the projection of the SNR symmetry axis runs from left to right. For all maps in tones of grey, lighter tones mean higher values.

4.1 Fully ordered MF and negligible FR

Let us begin by considering a completely ordered MF, aligned along the meridians, as from equations (56)–(59) with constant layer thickness. Let us also assume that the normalization A of the particle distribution is a constant (different functional dependencies with θ will also be used, then changing the relative importance of the emissivity, for instance, of the equatorial zone with respect to the polar ones).

At this stage, we take an observing frequency high enough that FR does not give any appreciable effect. The results are shown in Figs 7, 8, 9 and 10, respectively, for aspect angles of 0° (the

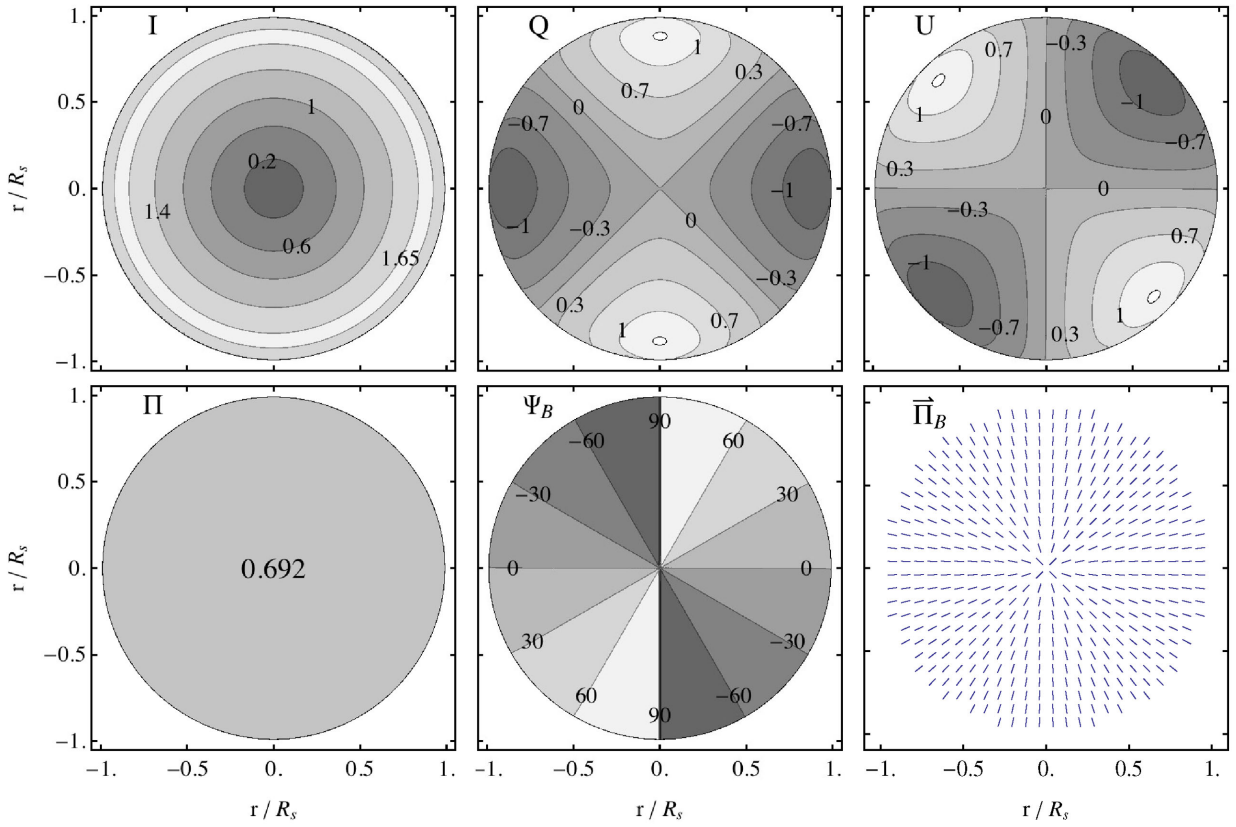

Figure 7. Fully ordered, meridionally oriented MF, without FR. Aspect angle of 0°. See text for the explanation of the panels.

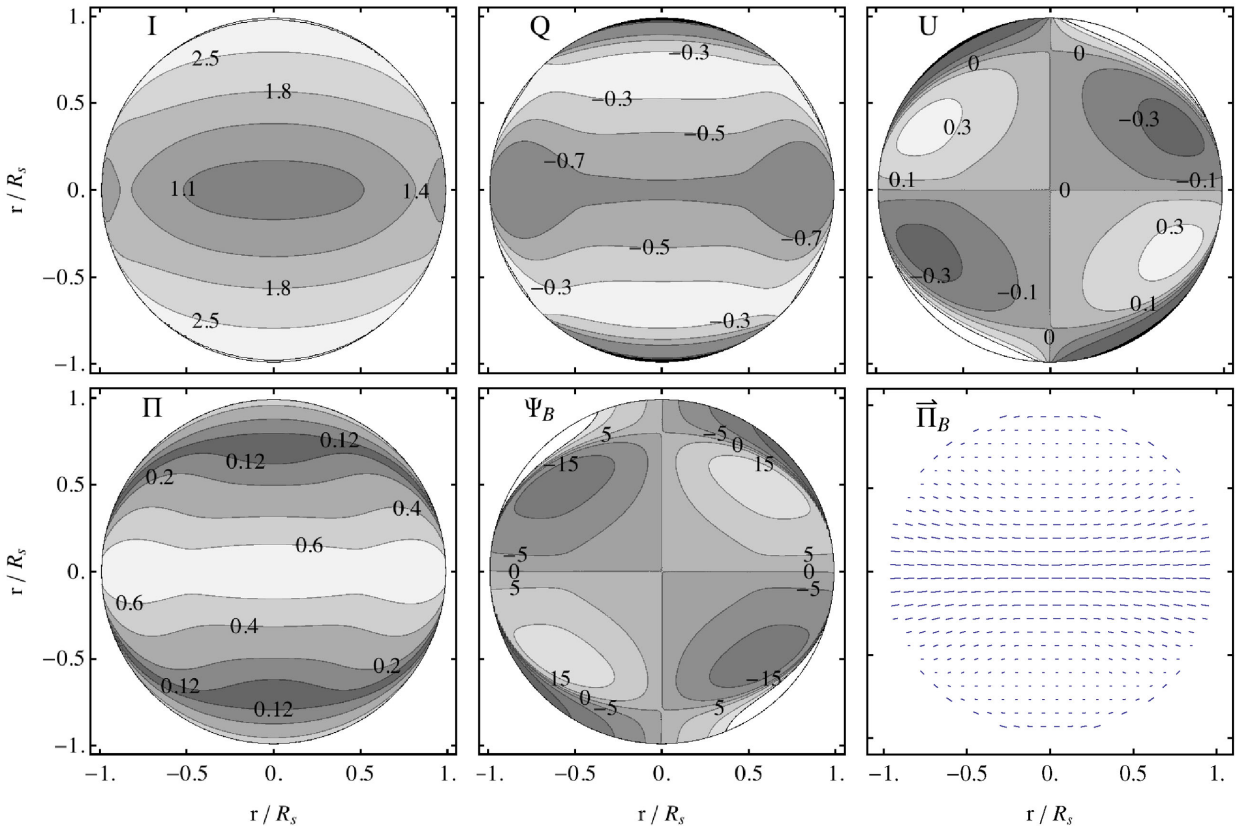

Figure 8. Fully ordered, meridionally oriented MF, without FR. Aspect angle of 30°.

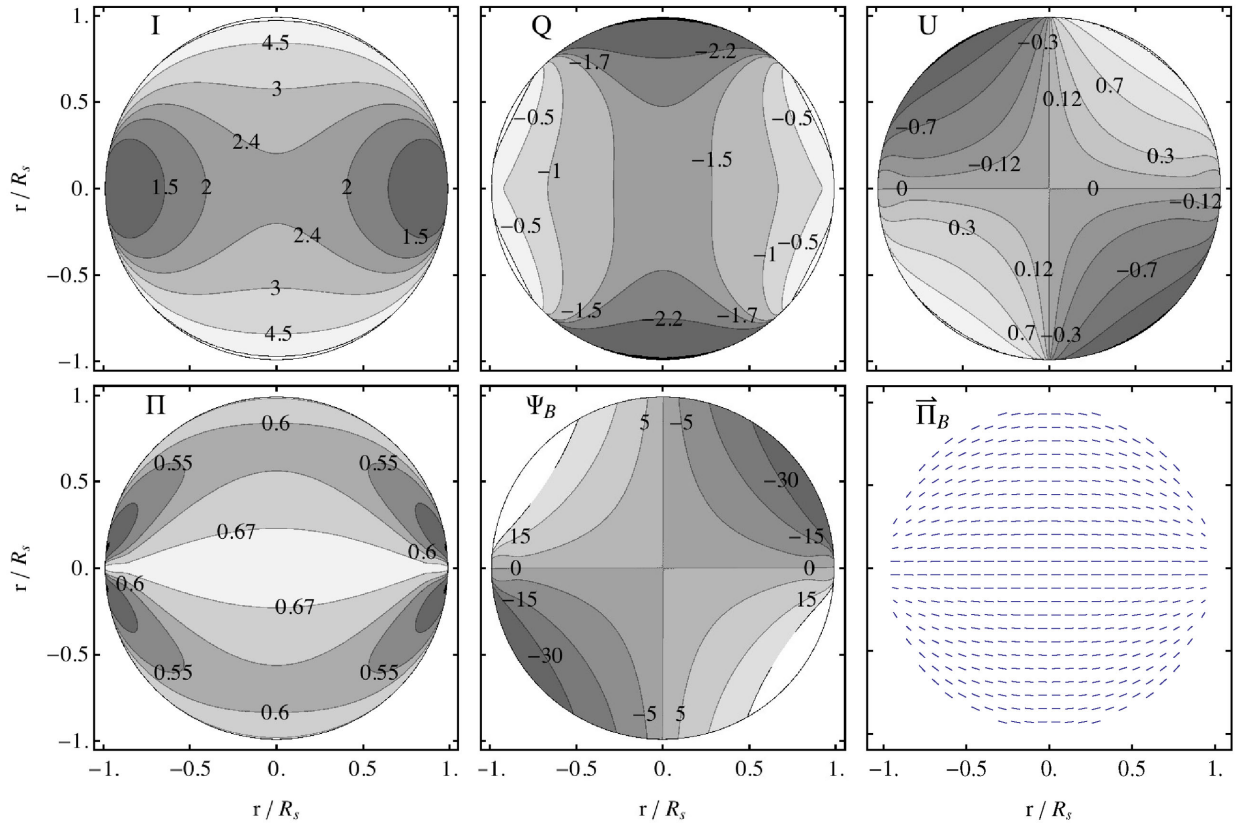

Figure 9. Fully ordered, meridionally oriented MF, without FR. Aspect angle of 60°.

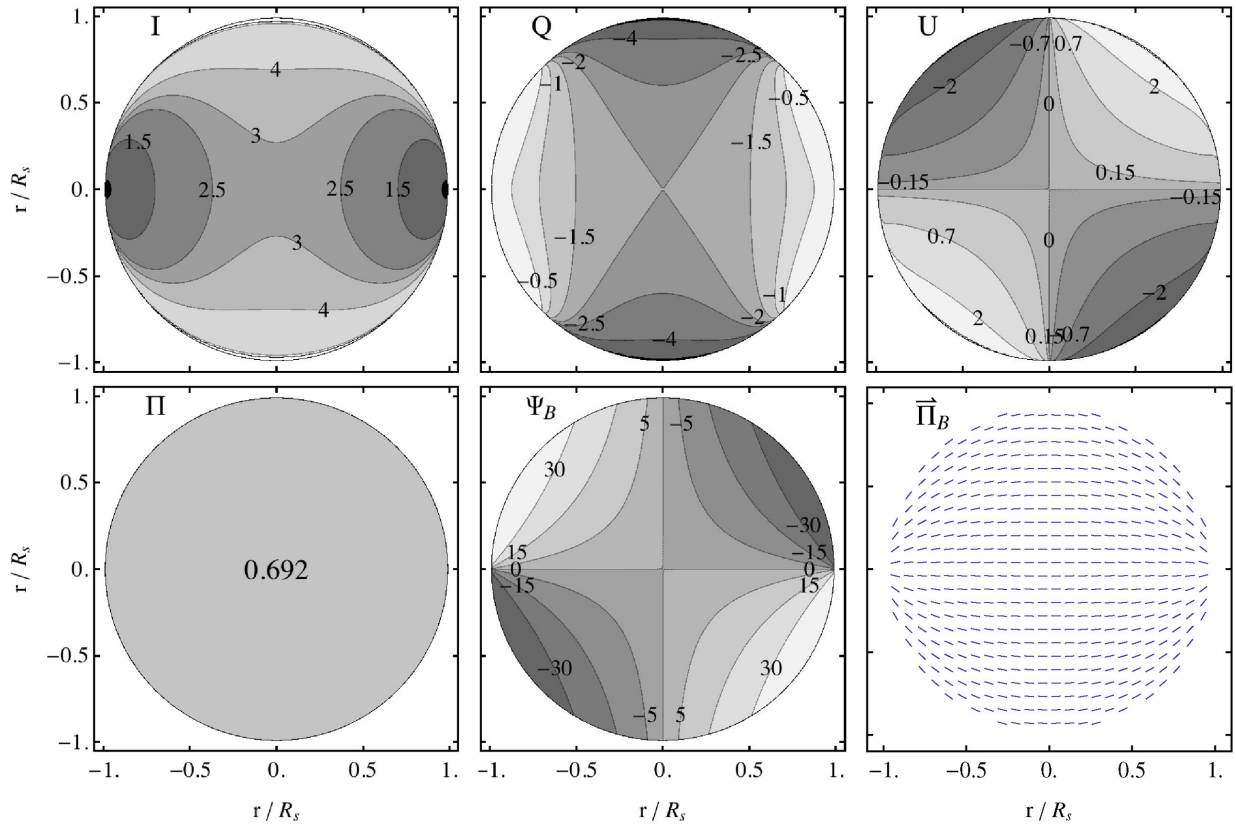

Figure 10. Fully ordered, meridionally oriented MF, without FR. Aspect angle of 90°.

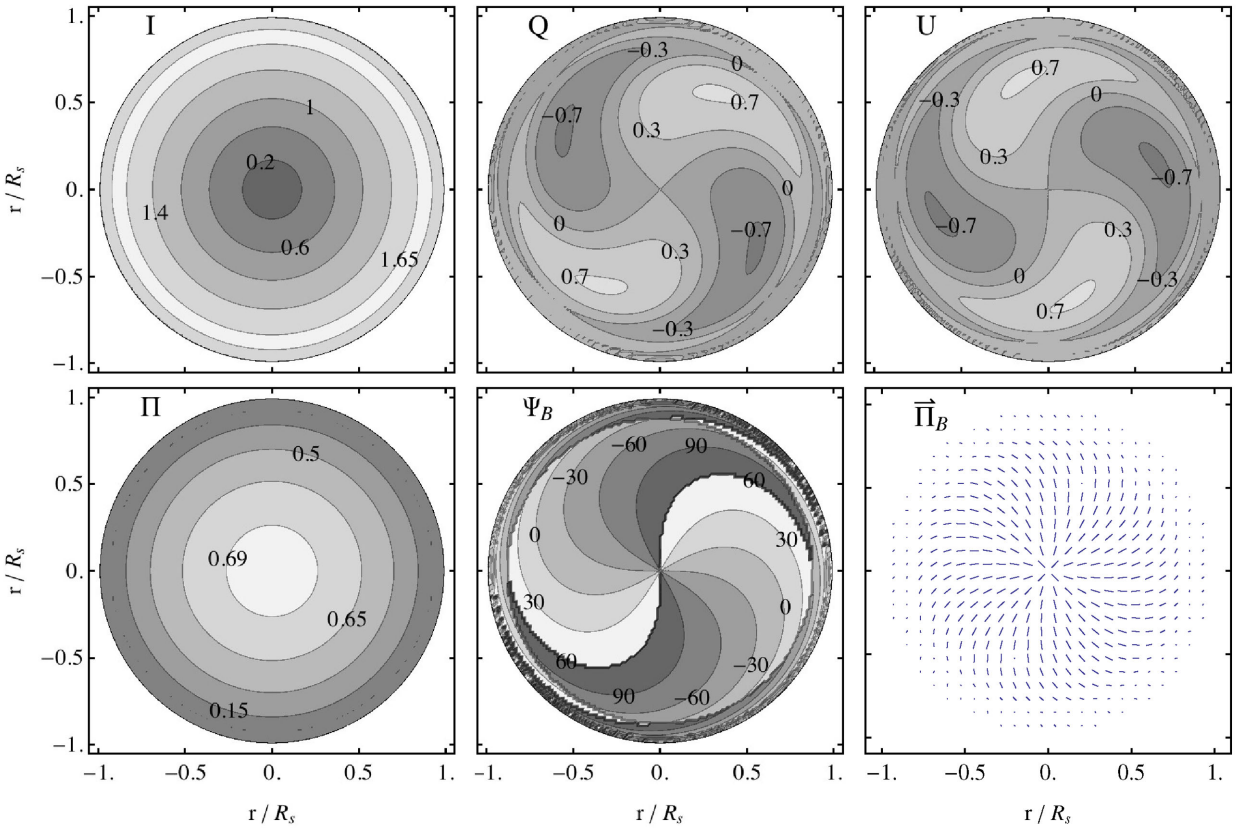

Figure 11. Fully ordered, meridionally oriented MF, with FR. Aspect angle of 0°.

polar direction), 30°, 60° and 90° (along the equatorial plane). This choice of aspect angles allows one to appreciate the continuity of the change of properties between the limit cases, even though they look so different from one another.

The three upper panels, from left to right, show the maps in the *I*, *Q* and *U* Stokes parameters. The three lower panels show more intuitive polarization quantities, namely, again from left to right, the polarization fraction, the magnetic polarization angle with respect to the projected axis and finally the vectorial map of the magnetic polarization.

In the 0° and 90° special cases, the direction of the projected MF in the front layer coincides with that in the rear layer. Therefore, in the absence of FR, the measured polarization is spatially constant, and reaches its maximum theoretical value (for all these maps, we have assumed $s = 2$, equivalent to a spectral index of -0.5 for the emission).

4.2 The effect of FR

In the same way as we did with the emission, let us use dimensionless quantities also for the treatment of FR. With reference to equation (63), let us normalize all RM quantities with:

$$\frac{e^3}{2\pi m_e^2 c^4} n_o B_o w, \tag{95}$$

where n_o is the electron density in the shell. In Figs 11, 12, 13 and 14, we can see the kind of distortion produced by FR. Here we have used an intermediate value of RM, namely to give FR equal to unity at the equator, when seen face on. The results are shown in Figs 11, 12, 13 and 14, respectively, for the same aspect angles of 0°, 30°, 60° and 90°. Also in this case, even though the patterns are distorted, one may appreciate the continuity in the change of pattern between contiguous aspect angles.

4.3 The effect of a random MF component

Let us consider here just the case in which in addition to the ordered MF, there is an isotropic random component, in which case the emission quantities derive from equations (26) and (27). While there is an infinity of possible cases, here we shall just consider the simplest one (even though not physically more justified than others), in which the $\sigma/\bar{B}$ ratio is constant everywhere. Moreover, with the aim of discussing the various effects independently, let us consider here just the case with vanishing FR. For an isotropic random MF component, a constant $\sigma/\bar{B}$ ratio means that on the projected MF, the effect of fluctuations will be larger when the ordered MF is oriented closer to the line of sight, and therefore, the depolarization level will be higher in those cases. The effect is more evident at large aspect angles, so that in Fig. 15 we present the case at an aspect angle of 90° (and $\sigma/\bar{B} = 1$). This map should be compared with Fig. 10.

4.4 Structure of RM maps

In the previous sections, we made a distinction between the standard definition of the RM (equation 64, which can be associated with real observations only for FR of a background source), and the RM (plus depolarization) that can actually be derived from observations for intrinsic FR (see equations 82 and 83). Figs 16 to 18, associated respectively with Figs 12 to 14, show these FR-related quantities.

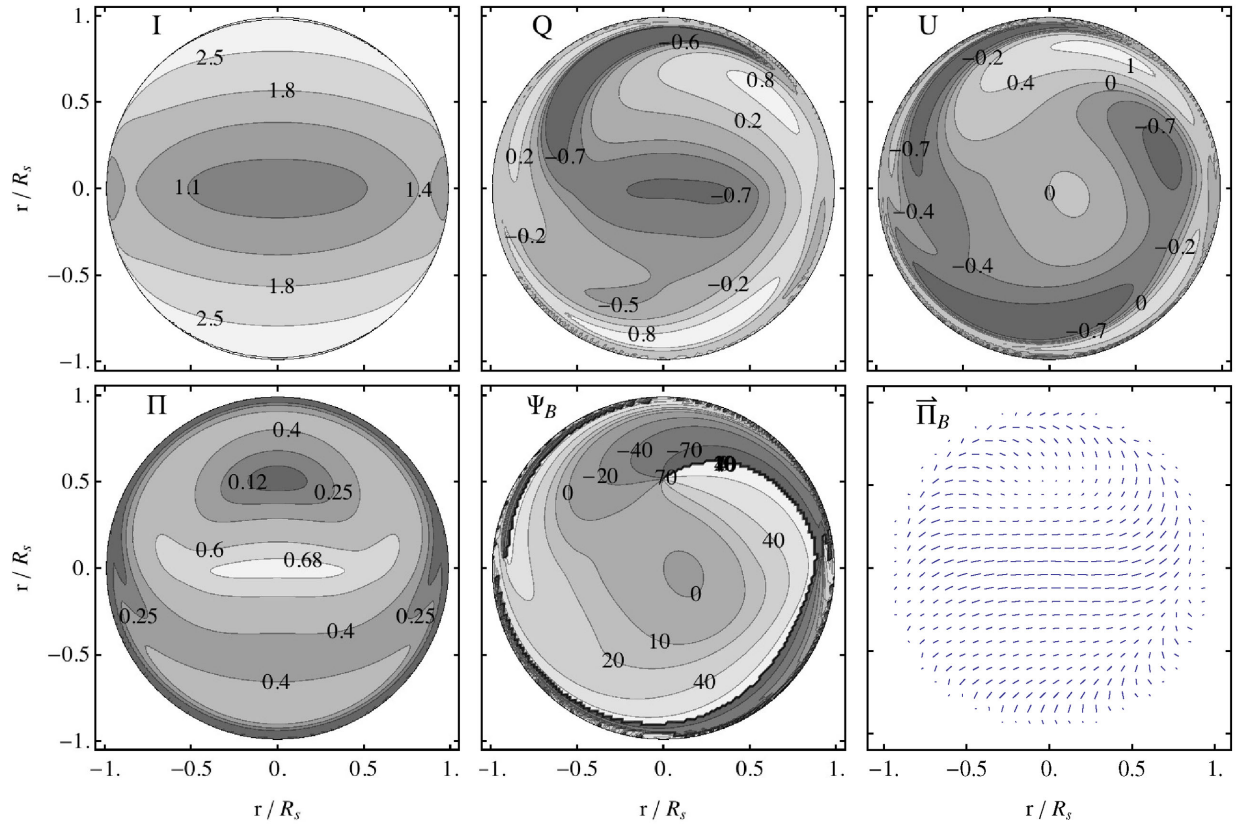

Figure 12. Fully ordered, meridionally oriented MF, with FR. Aspect angle of 30°.

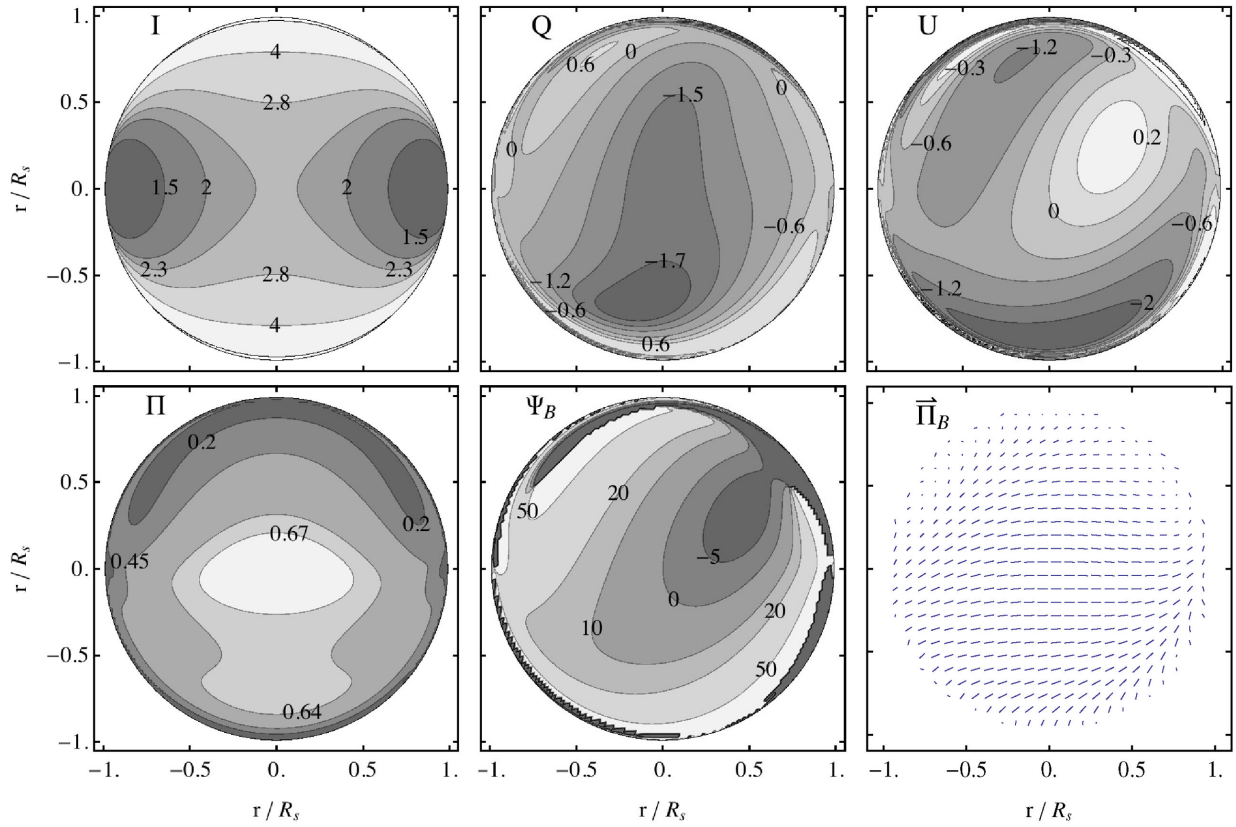

Figure 13. Fully ordered, meridionally oriented MF, with FR. Aspect angle of 60°.

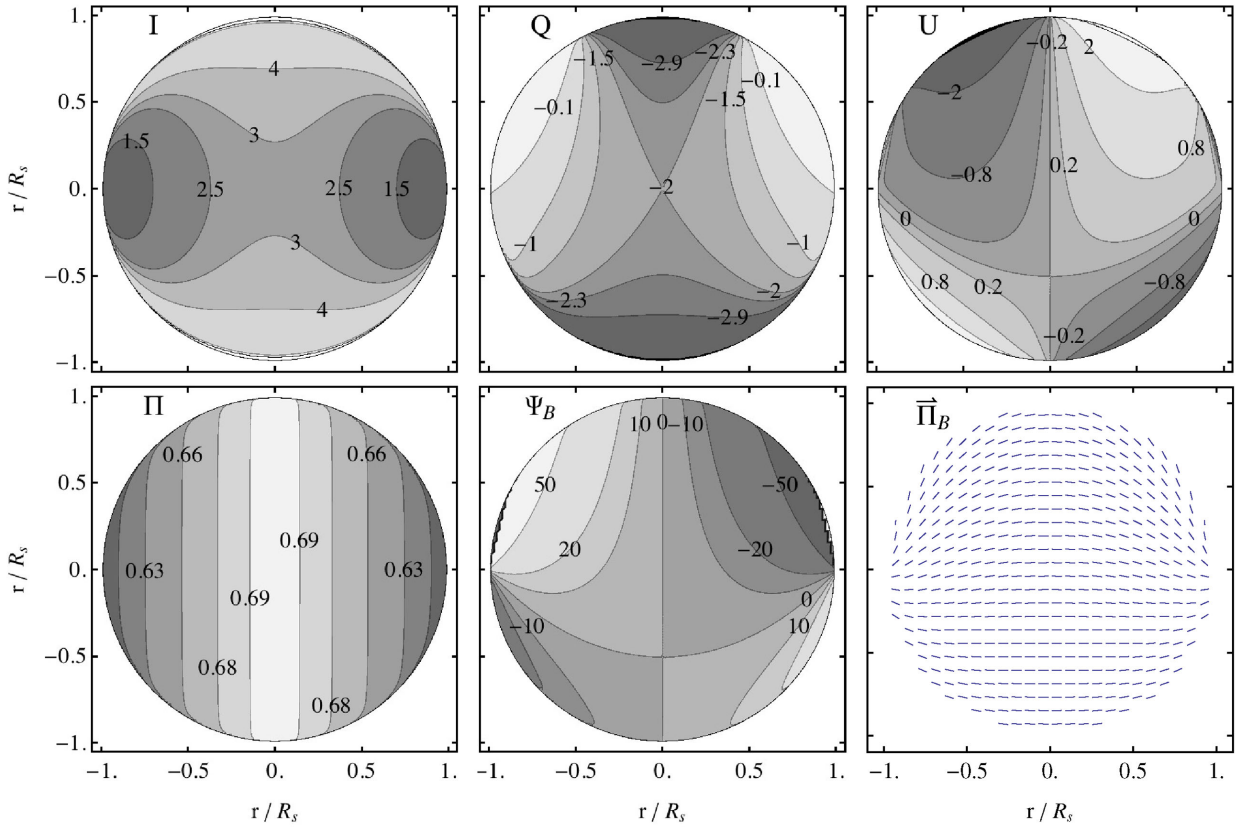

Figure 14. Fully ordered, meridionally oriented MF, with FR. Aspect angle of 90°.

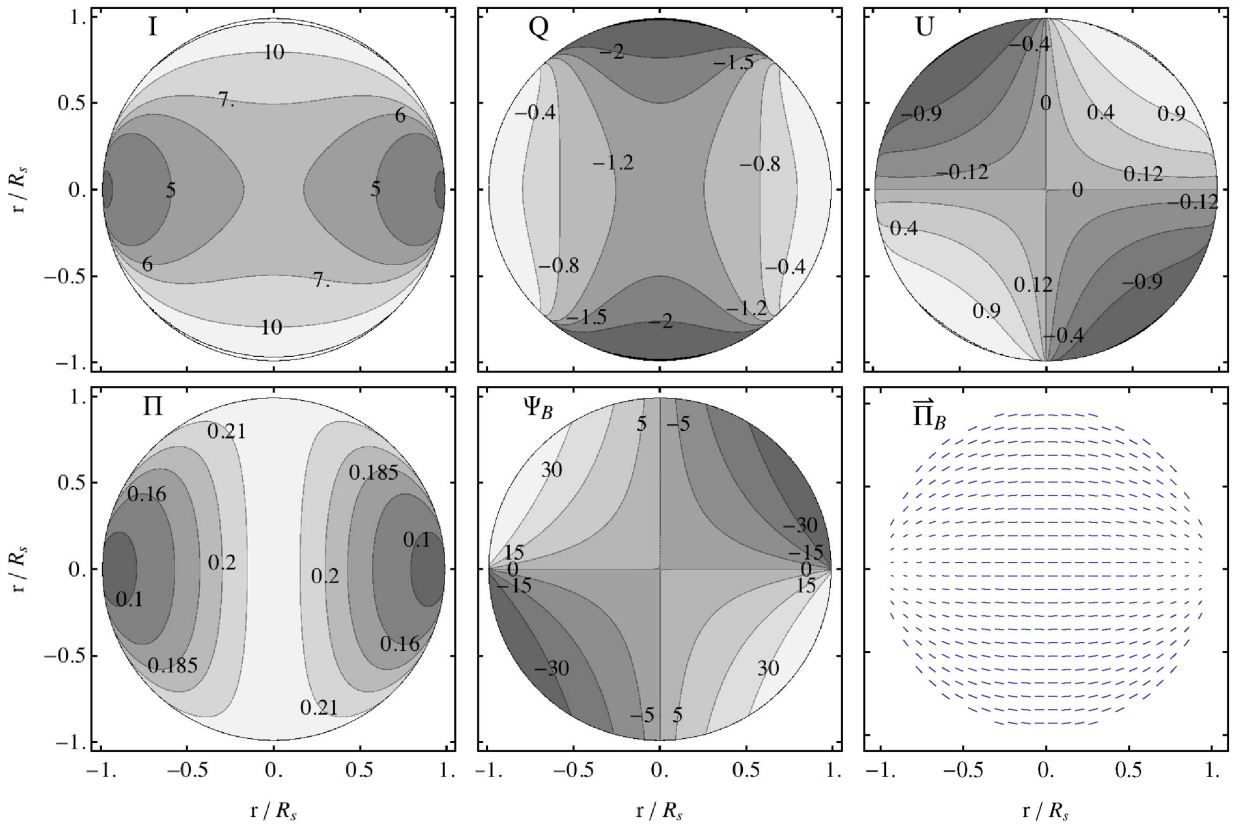

Figure 15. Fully ordered, meridionally oriented MF, with $\sigma/\bar{B} = 1$. Aspect angle of 90°.

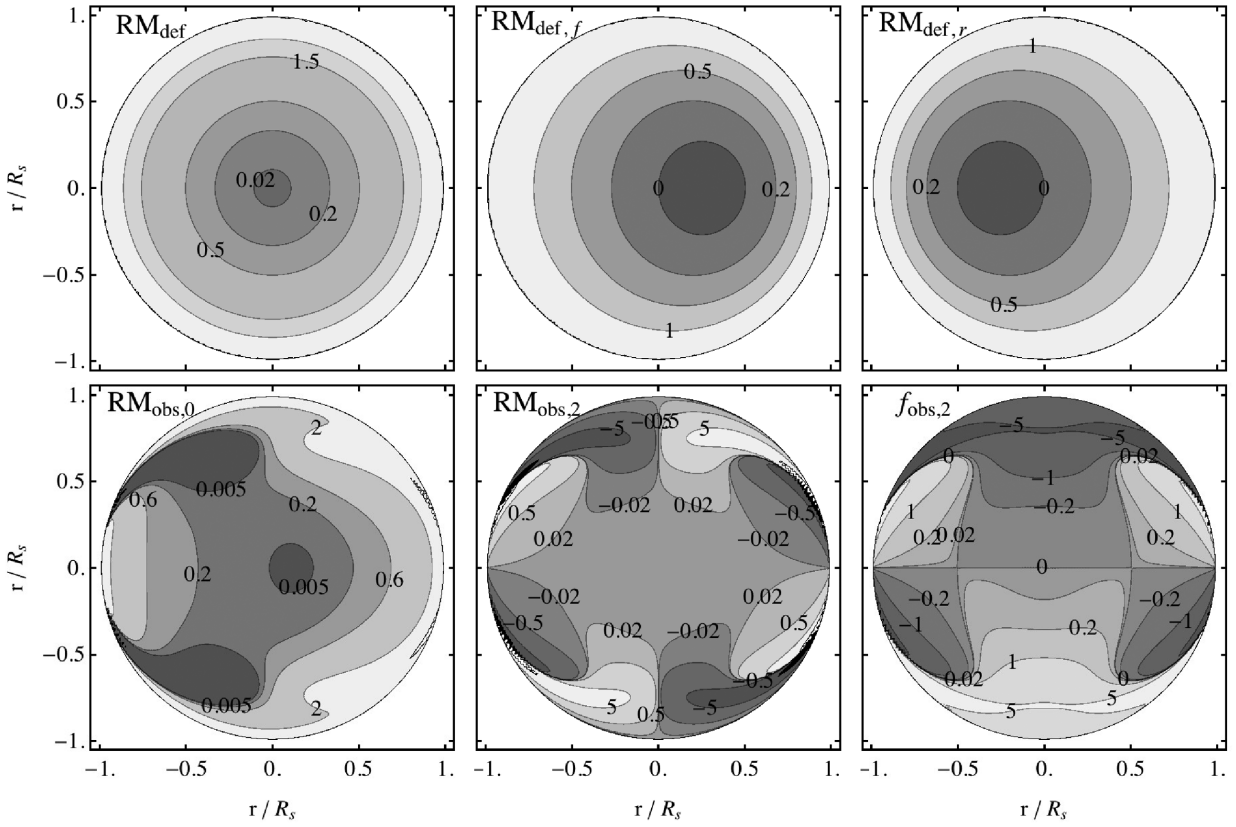

Figure 16. FR-related quantities, for the case shown in Fig. 12. Aspect angle of 30°.

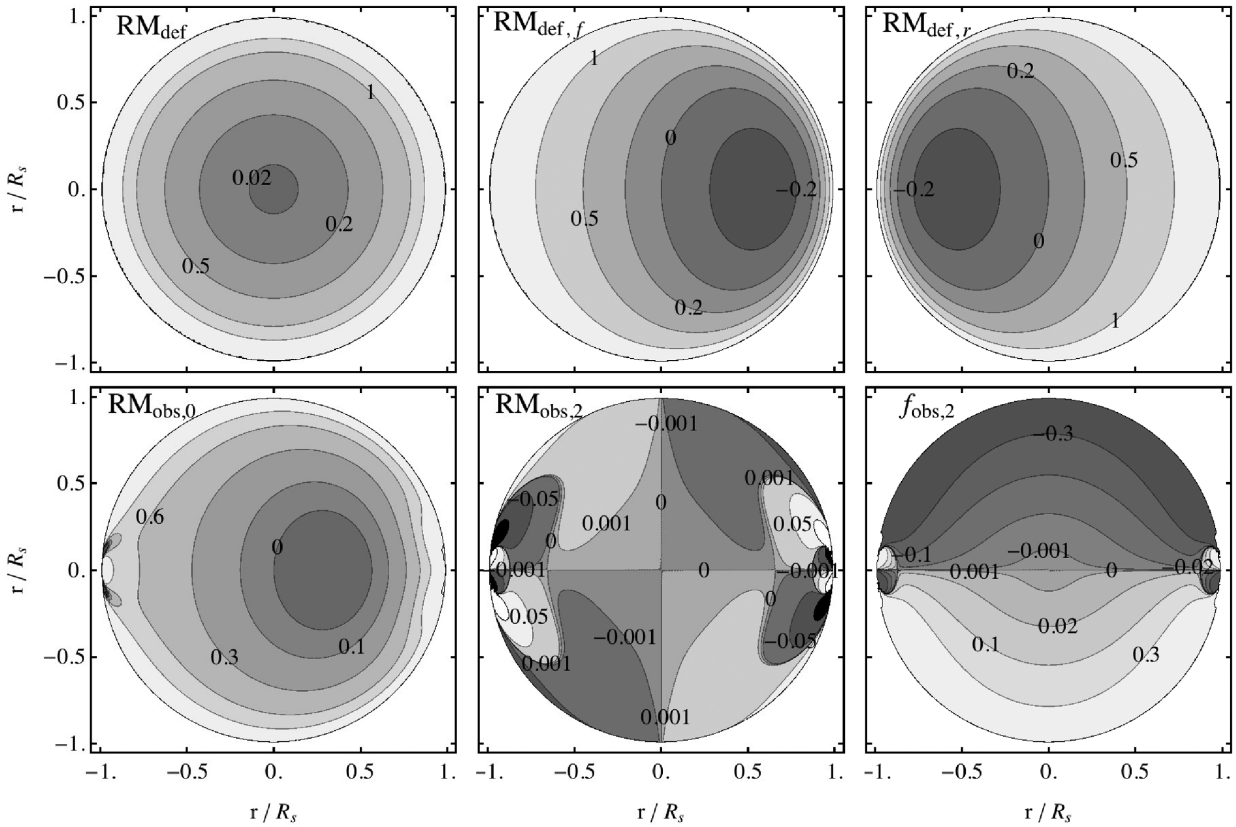

Figure 17. FR-related quantities, for the case shown in Fig. 13. Aspect angle of 60°.

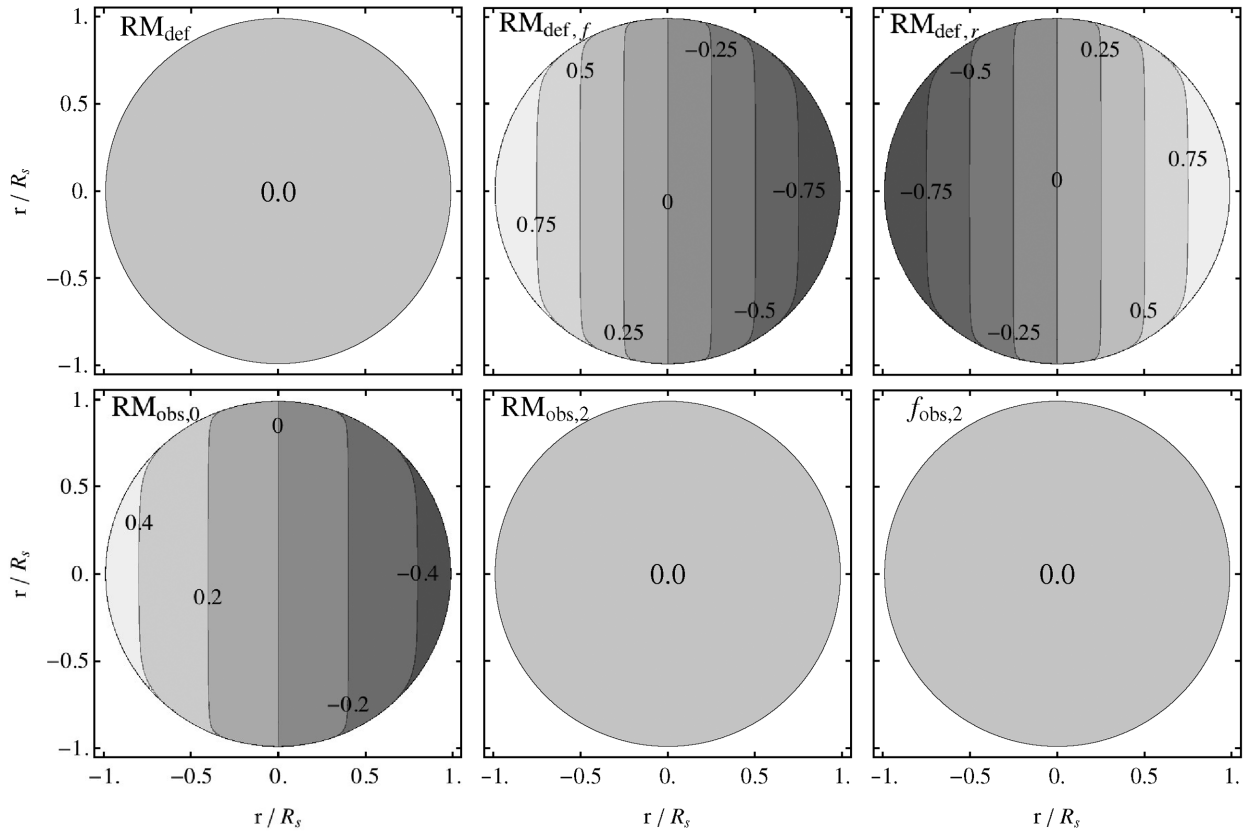

Figure 18. FR-related quantities, for the case shown in Fig. 14. Aspect angle of 90°.

In the upper panels, the RM is from the standard definition, namely (from left to right) its total value, the value for the front layer and that for the rear layer. The lower panels (again from left to right) show the observed map of the intrinsic RM (more precisely $\mathrm{RM}_{\mathrm{obs},0}$, its small λ limit), and then the quantities tracing the next order of approximation effects on the polarization direction ($\mathrm{RM}_{\mathrm{obs},2}$; the coefficient of λ^2, in equation 83) and on the polarization degree ($f_{\mathrm{obs},2}$; the coefficient of λ^2, with positive sign, in equation 82).

The next order of approximation effects, which to our knowledge has not been measured as yet, should be observable with high-quality and high-resolution observations at low-frequency radio wavelengths. Testing their patterns would provide further information to constrain the structure of a radio SNR. We may see that, at an aspect angle of 90°, the second-order terms vanish. In general, one may always expect them to vanish when the intrinsic polarization angles of the front and rear layers are equal, which implies that the quantity QU_{m} (defined right after equation 83) vanishes.

5 POLAR-CAPS VERSUS BARREL-LIKE MODELS

So far we have considered the simplest possible case, namely one in which the shocked ambient medium is confined to a shell of constant thickness, the MF into that shell is just the result of the ambient field compression and the normalization of the particle energy spectrum is the same everywhere.

Let us release now the last assumption and, following Fulbright & Reynolds (1990), let us parametrize the acceleration efficiency with the obliquity angle, namely the angle between the shock normal and the (ordered component of the) MF. Consistent with what is typically assumed in the literature, we will consider here the angle between the shock velocity and the post-shock MF (θ_{Bn2}), which is linked to the polar angle by the relations

$$\sin\theta_{Bn2} = \frac{\kappa\sin\theta}{\sqrt{\kappa^2\sin^2\theta+\cos^2\theta}} \tag{96}$$

and

$$\cos\theta_{Bn2} = \frac{\cos\theta}{\sqrt{\kappa^2\sin^2\theta+\cos^2\theta}}. \tag{97}$$

Incidentally, the polar angle θ coincides with the angle between the shock velocity and the ambient MF, θ_{Bn1}.

Let us also define as quasi-parallel and quasi-perpendicular cases those in which the normalization of the particle energy distribution is respectively proportional to $\cos^2\theta_{Bn2}$ (therefore, enhancing the emissivity at obliquity angles closer to 0°) or to $\sin^2\theta_{Bn2}$ (which privileges angles closer to 90°). In the former case, the emission will then be enhanced near the polar regions (the polar-cap morphology), while in the latter it is enhanced around the equatorial regions (the barrel-like morphology). Critical comparisons of these two morphologies are present in the literature, when discussing the nature of bilateral SNRs in general (e.g. Fulbright & Reynolds 1990; Orlando et al. 2007), or more specifically SN 1006 (e.g. Schneiter et al. 2010; Bocchino et al. 2011; Schneiter et al. 2015).

In fact, the quasi-perpendicular prescription leads to maps very similar to those of the isotropic case. Equation (96) gives values very close to unity, except in narrow regions around the poles. The opposite is for equation (97), which leads to polar-cap enhanced emission, and for which one can easily appreciate the differences (see, for instance, Fig. 19, for an aspect angle of 90°, to be compared with Fig. 10).

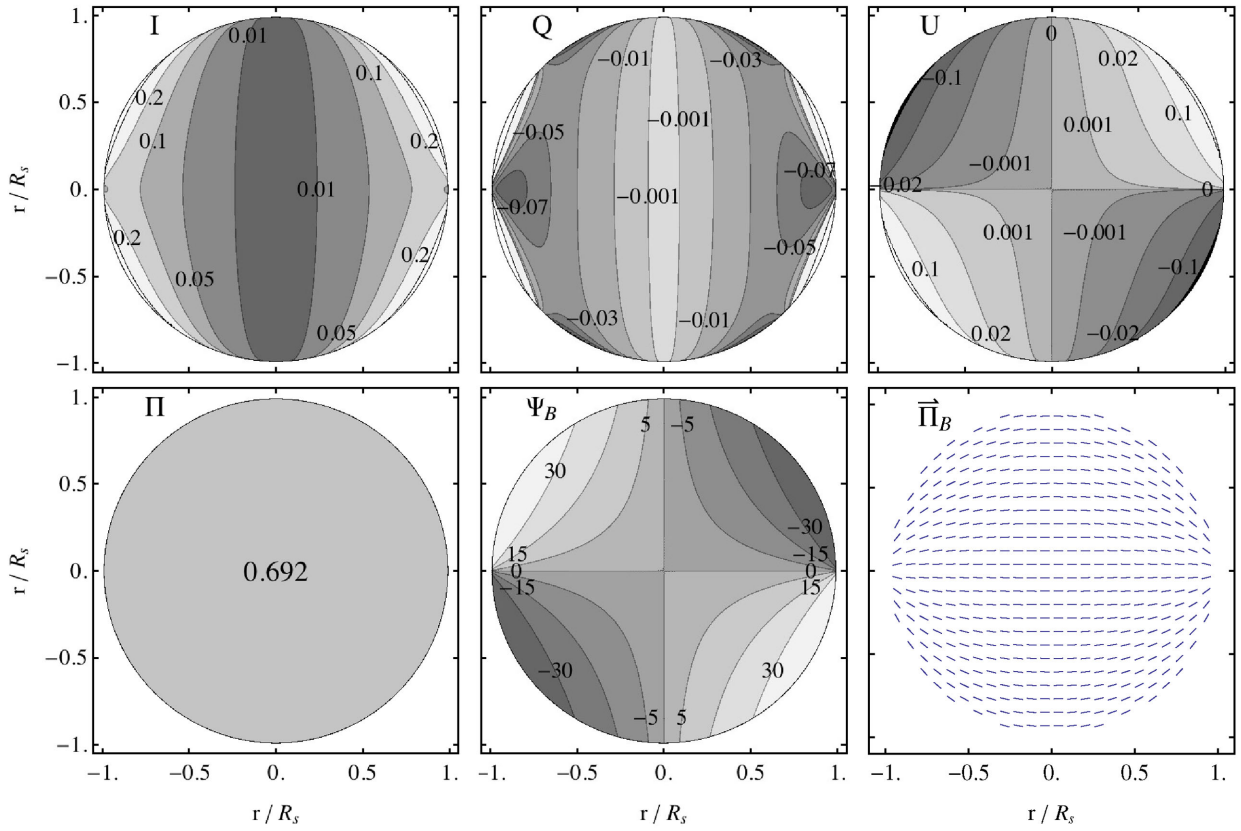

Figure 19. Meridionally oriented MF, with quasi-parallel injection efficiency. Aspect angle of 90°.

We have already mentioned that, for young SNRs, there is an indication that the MF configuration must be mostly radial. Our main intention here, far from presenting specific and detailed models for individual SNRs, is to show in general how radio polarization data could be effectively used to investigate similar objects. However, as an illustration, we shall consider here as an archetypal case the remnant of SN 1006, which has been extensively studied, and for which very detailed radio emission and polarization maps are now available.

Polarization mapping of this source (see, e.g., Reynolds & Gilmore 1993) shows that the direction of the projected MF is approximately radial along the two brighter limbs (in the north-east and south-west sectors). This pattern of polarization is clearly inconsistent with a quasi-perpendicular model (if the MF stays ordered and the internal FR is negligible), as shown, for instance, by Schneiter et al. (2015), and may be easily inferred from our Fig. 10. Instead, an ambiguity may remain between a quasi-parallel case with ordered MF, and either a quasi-parallel or a quasi-perpendicular case, but with the formation of radial MF patterns (possibly due to the onset of instabilities), especially in the brighter regions.

More recently, Reynoso, Hughes & Moffett (2013) showed that the polarization along the two fainter edges of SN 1006 (in the south-east and north-west sectors) is consistent with a tangential MF, and that while the average fractional polarization of the two bright limbs is about 17 per cent, it typically increases along the weaker limbs. For instance, in the south-east sector it reaches a value of about 60 ± 20 per cent (this last value being consistent with the theoretical limit of $\simeq$ 71 per cent, for a radio spectral index $\simeq$ 0.6). Reynoso et al. (2013) interpret these results in the framework of the quasi-parallel case, and in addition take the lower polarization fraction in the two brighter limbs as the signature of efficient particle acceleration and generation of magnetic turbulence in those regions.

However, in Section 2.3 we have shown that, for strong turbulence with an isotropic random MF in the upstream, the shock compression would imply strong anisotropy in the immediate downstream turbulence, leading anyway to large polarization fractions ($\simeq$ 60 per cent for typical radio spectral indices, see Fig. 5), with a polarization consistent with a preferential MF direction tangent to the shock front. Therefore, except for very finely tuned conditions, the observation of typically radial patterns for the projected MF seems to require the onset of Rayleigh–Taylor-like instabilities, and for this reason, we are going here to examine the effects of a preferentially radial MF, in the framework of a barrel-like model.

For simplicity, we shall consider here a monopole-like configuration for the ordered MF. The radially oriented MF may actually have alternate orientations in different places, but this affects neither the magnitude of the synchrotron emissivity nor its polarization. Like the standard quasi-perpendicular model, we shall also use here the $B \propto \sin\theta$ prescription, but, differently from before. Here, the only justification is that in this way the azimuthal dependence of the radio emission in SN 1006 can be roughly reproduced. To normalize the particle energy distribution, we will use again the $\sin^2\theta_{Bn2}$ prescription, as in the standard quasi-perpendicular case.

In Fig. 20, we show the Stokes parameters and the polarization in the absence of FR, with an aspect angle of 60° (see Petruk et al. 2009, for estimates of the aspect angle for SN 1006). On the other hand, if as mentioned above the radial MF reverses its orientation many times on smaller scales, one should not be able to detect any net effect of this radial pattern on the FR. Only the FR originating from the meridional structure would not average to

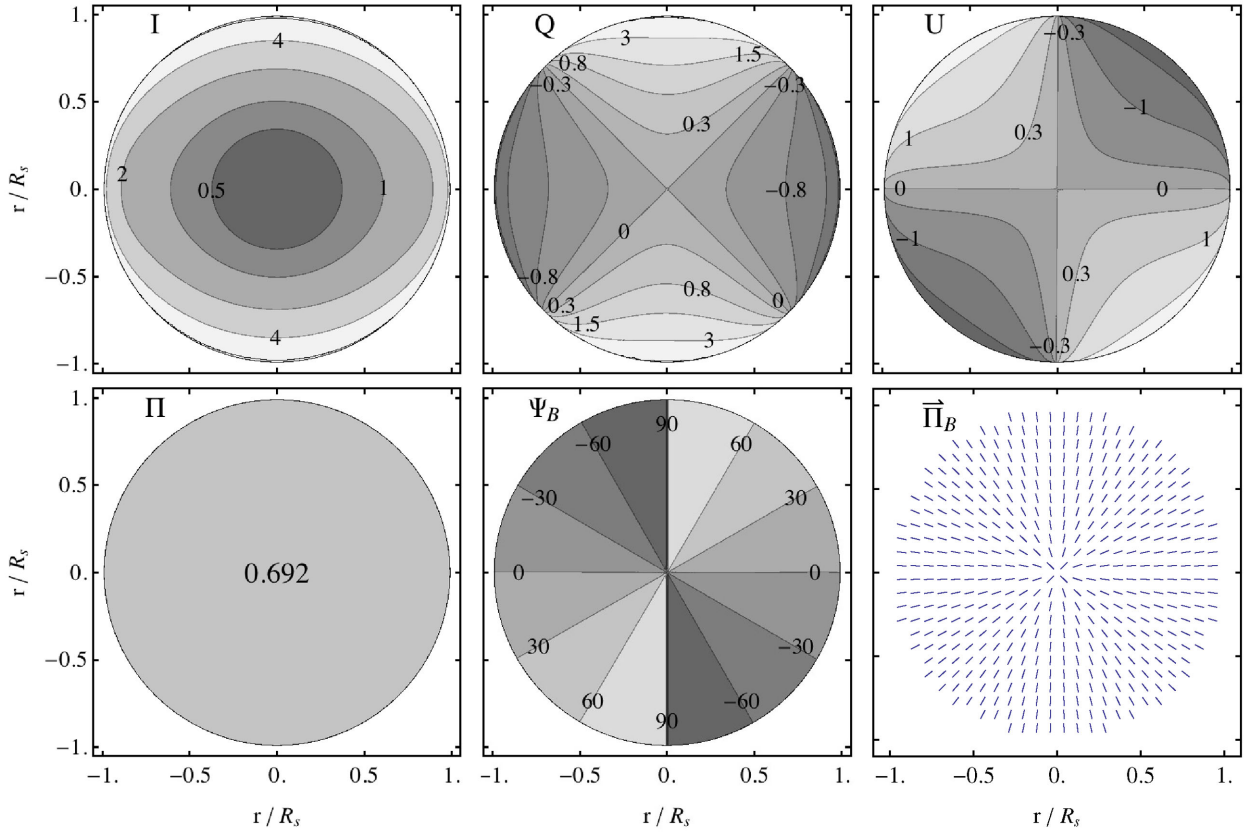

Figure 20. Radial MF with magnitude $\propto \sin\theta$ and a quasi-perpendicular distribution of particles, as seen at an aspect angle of 60°.

zero. A strategy to determine the correct model could then involve an analysis of the pattern of the internal RM to identify the symmetry axis of the underlying meridional MF. In fact, the pattern of the RM, independently of the distribution of the emitting particles, would allow one to identify the symmetry axis of the MF meridional component (see, e.g., Figs 17 or 18 for cases with large aspect angles). Therefore, if an overall gradient of the RM is detected, it may indicate the direction of the axis of symmetry of the SNR, and therefore, if the radio emission from this source shows a bilateral structure it would be interesting to check whether the two directions are nearly parallel or nearly orthogonal. Of course, this kind of analysis requires the absence of gradients in the foreground FR (to be checked by observing nearby polarized background sources) as well as a not too distorted structure for the SNR therefore this limits the number of objects on which such an analysis could actually be performed.

Finally, let us discuss the implications of the argument presented by Rothenflug et al. (2004) to disprove a barrel-like emission structure. Stated in a qualitative way, they noted that in a symmetric barrel-like structure, one can quantify a lower limit to the ratio of the emission near the projected centre of the SNR and from the projected limbs. More formally, they first considered a homogeneously emitting annulus of radius r, and defined $\mathcal{R}_\lambda$ (here, following the notation in Rothenflug et al. 2004, the symbol λ is an angle) as the ratio between the flux of the regions whose projected distance from the symmetry axis is less than $r\sin\lambda$, and those with projected distance larger than $r\sin\lambda$. In this case, by purely geometrical arguments, this ratio is found to be equal to $\pi/(2\lambda) - 1$. In particular, the authors use $\lambda = \pi/3$, for which the ratio evaluates to 0.5. Their last point is that a generic distribution of the emission can be imagined as the sum of more annuli, with different radii, in which case using that criterion for the largest radius gives a lower limit to the global ratio $\mathcal{R}_{\pi/3} > 0.5$.

Rothenflug et al. (2004), in the derivation of their criterion, used the assumption of isotropic radiation (cf. their section A.1). This assumption, while apparently reasonable, in fact, requires the MF to be completely random and, among others, it would be inconsistent with the presence of polarized emission, as actually observed. On the other hand, if we release this assumption, the situation can change considerably. In particular, Fig. 21 shows an annulus seen edge on (now the orientation matters), for different values of the ratio between the random and ordered (radial) MF, for some choices of the spectral index. It is apparent that, while the asymptotic limit for large $\sigma/\bar{B}$ values is 0.5, independently of the slope s, lower values are obtained for non-negligible values of the ordered component.

More insight can be obtained by computing the equatorial radial profile for the model shown in Fig. 20 (with an aspect angle of 60°), for different values of $\sigma/\bar{B}$. It can be seen (Fig. 22) that, while the emission near the projected centre is appreciable for large $\sigma/\bar{B}$ values (mostly random MF), in the limit of a completely ordered radial MF ($\sigma/\bar{B} = 0$), it vanishes. In the lower panel of the same figure we show the profile of the fractional polarization. In the bright limbs of SN 1006, a polarization fraction of ∼20 per cent is measured (Reynolds & Gilmore 1993; Reynoso et al. 2013). This poses an upper limit of $\simeq 1$ to $\sigma/\bar{B}$. Therefore, the actual profile should be somehow dimmer near the centre than what is estimated for a purely random MF.

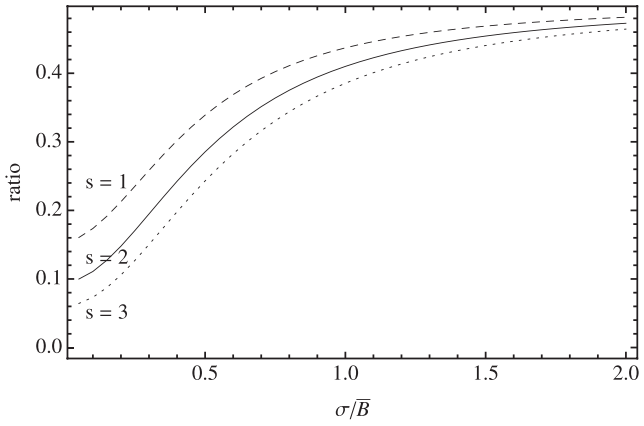

Figure 21. The Rothenflug et al. (2004) criterion, generalized to a radially oriented ordered MF plus a random MF component.

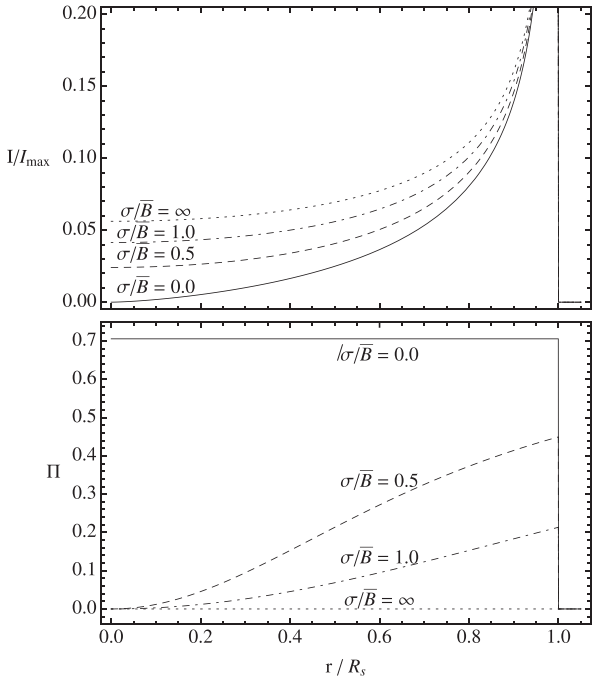

Figure 22. Profiles for a model with radial MF with magnitude $\propto \sin\theta$, quasi-perpendicular distribution of particles (barrel-like model), and different values of $\sigma/\bar{B}$, as seen at an aspect angle of 60°. Upper panel: Normalized I flux profiles, for an equatorial cut. Lower panel: Profiles of the polarization fraction, for the same cases.

To give a closer comparison with the radio profiles shown in Rothenflug et al. (2004), in Fig. 23 we also present the profiles of the flux, integrated along the direction orthogonal to the projected equator. In this case, the differences between models with different $\sigma/\bar{B}$ values are less evident, but still exist. In particular, one may see from Fig. 23 that, in the fully ordered MF case, the integrated I value on the symmetry axis is just about 40 per cent of the Rothenflug et al. (2004) case (i.e. $\sigma/\bar{B} = \infty$). Therefore, the criterion introduced in that paper cannot be intended by itself as a mathematical proof against a barrel-like geometry. In fact, for a radially oriented ordered component of the MF, it would be oriented almost along the projection plane near the limbs and towards the observer near the centre, and this may result in smaller values of the ratio of emission between centre and limbs.

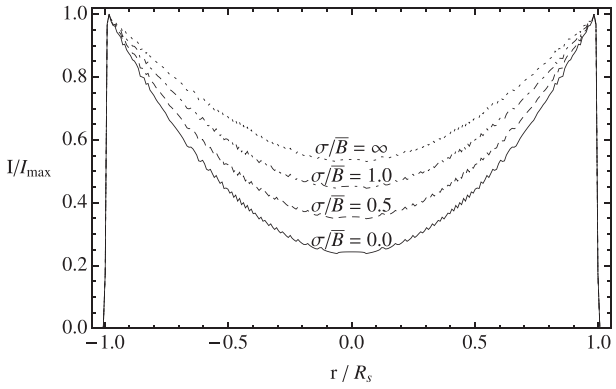

Figure 23. Normalized I flux profiles, integrated along the directions perpendicular to the equator, for the same models as in Fig. 22.

6 SUMMARY

In this paper, we have presented a generalization of the classical treatment of the synchrotron radiation, valid for when the MF has a random component. The resulting formulae, while nicely resembling those in the classical case, are now valid for any relative level between ordered and random components, and clearly show that the emission for a partially random case cannot be simply modelled as the sum of the emission in a fully ordered MF and that in a completely random MF.

We have then used these formulae to model the synchrotron emission from shell-type SNRs. The main limitation of the present treatment is its applicability only when the particle energy distribution is a power law, and for this reason, we have focused our attention on the radio emission in SNRs. For the future, we plan to extend this treatment also to particle energy distributions with an upper cut-off to allow also an analysis of the non-thermal SNR emission in the X-ray energy range. Another limitation of this treatment is that the fluctuations considered are on scales smaller than the instrumental resolution. For fluctuations on larger scales, the only possible approach is through multidimensional, high-resolution fully numerical simulations.

Our goal here is to allow a numerically much lighter treatment than full simulations, while still keeping enough detail to allow investigations of several effects. With this aim, to model the emission from shell-type SNRs, we have introduced a thin-shell model. Our discussion has involved various issues, like the dependence of the typical polarized fractions on the level of MF fluctuations, and the pattern of the polarization as well as of the RM on the geometry of the ordered MF component. We have also introduced the idea that in the presence of internal FR, the measured RM maps contain information different from that of the classical case, when FR is just due to a foreground medium. In addition, we have also discussed further effects, on the observed direction of the polarization as well as on its level, which should be more evident at longer radio wavelengths and which, if suitably tested in the future, could provide additional information on the MF structure.

While this paper has been mostly devoted to a meridional geometry of the ordered MF, as one would expect for a laminar expansion into an ambient medium with a pre-existing homogeneous MF, having in mind young SNRs, and SN 1006 in particular, we have also discussed a radially oriented MF. We have shown that the radial profiles of the emission may effectively depend also on the level of MF fluctuations, so that for a low level of fluctuations, also a barrel-like geometry of the emissivity could be consistent with the

lower surface brightness near the central regions of the projected image.

ACKNOWLEDGEMENTS

We thank the referee, Dr P. F. Velázquez, for his careful reading and a number of suggestions and corrections that helped us to improve the paper considerably. This work is partially funded by the PRIN INAF 2010 and by the CNRS-INAF PICS 2012.

REFERENCES

Bocchino F., Orlando S., Miceli M., Petruk O., 2011, A&A, 531A, 129
Caprioli D., Spitkovsky A., 2014a, ApJ, 783, 91
Caprioli D., Spitkovsky A., 2014b, ApJ, 794, 46
Dickel J. R., Milne D. K., 1976, Aust. J. Phys., 29, 435
Dubner G., Giacani E., 2015, A&AR, 23, 3
Fulbright M. S., Reynolds S. P., 1990, ApJ, 357, 591
Inoue T., Shimoda J., Ohira Y., Yamazaki R., 2013, ApJ, 772, L20
Jun B.-I., Norman M. L., 1996, ApJ, 472, 245
Kothes R., Fedotov K., Foster T. J., Uyaniker B., 2006, A&A, 457, 1081
Milne D. K., 1987, Aust. J. Phys., 40, 771
Orlando S., Bocchino F., Reale F., Peres G., Petruk O., 2007, A&A, 470, 927
Petruk O. et al., 2009, MNRAS, 393, 1034
Petruk O., Kuzyo T., Beshley V., 2016, MNRAS, 456, 2343
Pohl M., Wilhelm A., Telezhinsky I., 2015, A&A, 574, 43
Reynolds S. P., Gilmore D. M., 1993, AJ, 106, 272
Reynoso E. M., Hughes J. P., Moffett D. A., 2013, AJ, 145, 104
Rothenflug R., Ballet J., Dubner G., Giacani E., Decourchelle A., Ferrando P., 2004, A&A, 425, 121
Rybicki G. B., Lightman A. P., 1979, Radiative Processes in Astrophysics. Wiley-Intersci., New York
Schneiter E. M., Vélazquez P. F., Reynoso E. M., de Colle F., 2010, MNRAS, 408, 430
Schneiter E. M., Vélazquez P. F., Reynoso E. M., Esquivel A., de Colle F., 2015, MNRAS, 449, 88

This paper has been typeset from a TEX/LATEX file prepared by the author.